

NOVEL ESTIMATION AND CONTROL TECHNIQUES IN
MICROMANIPULATION USING VISION AND FORCE FEEDBACK

by
HAKAN BİLEN

Submitted to the Graduate School of Engineering and Natural Sciences
in partial fulfillment of
the requirements for the degree of
Master of Science
Sabanci University
Spring 2008

NOVEL ESTIMATION AND CONTROL TECHNIQUES IN
MICROMANIPULATION USING VISION AND FORCE FEEDBACK

Hakan BİLEN

APPROVED BY

Assoc. Prof. Dr. Mustafa ÜNEL
(Thesis Advisor)

Assist. Prof. Dr. Kemalettin ERBATUR

Assist. Prof. Dr. Ahmet ONAT

Assist. Prof. Dr. Devrim GÖZÜAÇIK

Assist. Prof. Dr. Hakan ERDOĞAN

DATE OF APPROVAL:

©Hakan Bilen 2008
All Rights Reserved

Autobiography

Hakan Bilen was born in Izmir, Turkey in 1983. He received his B.S. degree in Mechatronics Engineering from Sabanci University, Istanbul, Turkey in 2006. His research interests include computer vision, estimation and control, robotics, visual servoing.

The following were published out of this thesis:

- H. Bilen, M. Unel, “Micromanipulation Using A Microassembly Workstation with Vision and Force Sensing”, *Springer Lecture Notes in Computer Sciences*, 2008 (in press)
- H. Bilen, H., Hocaoglu, M., Ozgur, E., Unel, M., Sabanovic, A., “A Comparative Study of Conventional Visual Servoing Schemes in Microsystem Applications”, *IEEE/RSJ International Conference on Intelligent Robots and Systems*, San Diego, 2007, pp. 1308–1313.
- M. A. Hocaoglu, H. Bilen, E. Ozgur, and M. Unel, “Model-Based vs. Model-Free Visual Servoing: A Performance Evaluation in Microsystems”, *IASTED International Conference on Robotics and Applications*, Germany, 2007.
- H. Bilen, M. Hocaoglu, E. Ozgur, M. Unel, “Gorsel Geri Beslemeli Kontrol Tekniklerinin Mikrosistem Uygulamalarinda Karsilastirilmesi”, *Turkiye Otomatik Kontrol (TOK) Ulusal Toplantisi*, Turkey, 2007.

Acknowledgments

It is a great pleasure to extend my sincere gratitude and appreciation to thank my thesis advisor, Assoc. Prof. Mustafa Ünel, who consistently believed in my skills and provided me the opportunity and liberty to work independently. His careness, support and guidance during my studies at Sabancı University were very precious.

Among all members of the Faculty of Engineering and Natural Sciences, I would gratefully thank Assist. Prof. Kemalettin Erbatur, Prof. Devrim Gözüaık, Assist. Prof. Ahmet Onat and Assist. Prof. Hakan Erdoğan for their interest in my work and spending their valuable time to serve as my jurors. I also wish to thank Prof. Asif Sabanovic for providing the experimental setup and valuable suggestions.

I would like to acknowledge the support provided by Sabancı University through the Internal Grant No. IACF06-00417.

Moreover, I would like to thank The Scientific & Technological Research Council of Türkiye (TÜBİTAK) for its support during my MS studies.

I would also like to thank every single member of Mechatronics Graduate Laboratory for being good companies during my graduate study. Many thanks to Muhammet, Emrah, Teoman, Kazim for their help and sharing all they know; Merve, Erol, Meltem, Ramazan, Nese, Caner, Islam, Abdullah for their friendship and all others I wish I had the space to acknowledge in person.

Finally, I would like to thank my family for all their love and support throughout my life.

NOVEL ESTIMATION AND CONTROL TECHNIQUES IN MICROMANIPULATION USING VISION AND FORCE FEEDBACK

Hakan BİLEN

Mechatronics Engineering, MS Thesis, 2008

Thesis Advisor: Assoc. Prof. Dr. Mustafa ÜNEL

Keywords: micromanipulation, microassembly, biomanipulation, visual servoing, estimation, optimal control, camera calibration

Abstract

With the recent advances in the fields of micro and nanotechnology, there has been growing interest for complex micromanipulation and microassembly strategies. Despite the fact that many commercially available micro devices such as the key components in automobile airbags, ink-jet printers and projection display systems are currently produced in a batch technique with little assembly, many other products such as read/write heads for hard disks and fiber optics assemblies require flexible precision assemblies. Furthermore, many biological micromanipulations such as invitro-fertilization, cell characterization and treatment rely on the ability of human operators. Requirement of high-precision, repeatable and financially viable operations in these tasks has given rise to the elimination of direct human involvement, and autonomy in micromanipulation and microassembly.

In this thesis, a fully automated dexterous micromanipulation strategy based on vision and force feedback is developed. More specifically, a robust vision based control architecture is proposed and implemented to compensate errors due to the uncertainties about the position, behavior and shape of the microobjects to be manipulated. Moreover, novel estimators are designed to identify the system and to characterize the mechanical properties of the biological structures through a synthesis of concepts from the computer vision, estimation and control theory. Estimated mechanical parameters are utilized to reconstruct the imposed force on a biomembrane and to provide the adequate information to control the position, velocity and acceleration of the probe without damaging the cell/tissue during an injection task.

MİKROMANİPÜLASYONDA GÖRME VE KUVVET TABANLI GERİBESLEMeye DAYALI YENİ KESTİRİM VE KONTROL TEKNİKLERİ

Hakan BİLEN

Mekatronik Mühendisliği, Yüksek Lisans Tezi, 2008

Tez Danışmanı: Doç. Dr. Mustafa ÜNEL

Anahtar Kelimeler: mikromanipülasyon, mikromontaj, biyomanipülasyon, görsel temelli kontrol, kestirim, optimal kontrol, kamera kalibrasyonu

Özet

Mikro ve nanoteknolojideki gelişmelerle birlikte kompleks mikromanipülasyon ve mikromontaj yöntemlerine olan ilgi büyüyerek artmaktadır. Otomobil havayastıklarındaki, püskürtmeli yazıcı kafalarındaki ve görüntülü projeksiyon sistemlerindeki anahtar komponentler gibi birçok ticari mikro aygıt, günümüzde az miktarda montaj içeren toplu üretim teknikleriyle üretilirken, sabit disk yazma/okuma kafaları ve optik entegreler gibi birçok başka mikro aygıtın üretimi içinse esnek hassas montaja ihtiyaç duyulmaktadır. Bunun yanında, yapay dölleme, hücre karakterizasyonu ve tedavisi gibi birçok biyolojik mikromanipülasyonun başarısı operatörlerin yeteneklerine bağlıdır. Bu uygulamalarda yüksek hassasiyette, tekrarlanabilir ve finansal açıdan uygulanabilir operasyonlara ihtiyaç duyulması mikromanipülasyon ve mikromontajda doğrudan insan müdahalesinin elenmesi ve özerkliğin artmasına neden olmaktadır.

Bu tezde, görüş ve kuvvet geribeslemesine dayalı tamamen otomatik hünarlı bir mikromanipülasyon stratejisi geliştirilmiştir. Özellikle mikro objelerin pozisyon, davranış ve şekillerindeki belirsizliklerinden kaynaklanan hataları gidermek için gürbüz görsel temelli kontrol mimarisi önerilmiş ve uygulanmıştır. Ayrıca kullanılan sistemi tanımlamak ve biyolojik yapıların mekanik özelliklerini karakterize etmek için bilgisayarla görme, kestirim ve kontrol senteziyle yeni kestiriciler tasarlanmıştır. Kestirilen mekanik parametreler bir enjeksiyon operasyonu sırasında biyomembrana uygulanan kuvveti yeniden kurmak ve probun pozisyon, hız ve ivme kontrolünü hücre/dokuya zarar vermeden sağlamak için kullanılmıştır.

Table of Contents

Autobiography	iv
Acknowledgments	v
Abstract	vi
Özet	vii
1 Introduction	1
1.1 Contributions of the Thesis	3
1.2 Outline of the Thesis	4
2 Micromanipulation	5
2.1 What is Micromanipulation?	5
2.2 Microassembly Workstation	8
2.3 Visual Servoing	12
3 Micromanipulation Using Vision & Force	16
3.1 Visual Feedback	16
3.1.1 Object and End Effector Detection	16
3.1.2 Real-Time Tracking	21
3.1.3 Visual Control Law	22
3.1.4 Autofocusing	23
3.2 Force Feedback	26
3.3 Path Planning for Collision-Free Transportation of Microobjects	27
3.3.1 Algorithm	28
4 Parameter Estimation Schemes Using Vision and/or Force	31
4.1 Background	31
4.2 Optical System Calibration	32
4.2.1 Selection of Calibration Pattern	36
4.2.2 Novel Calibration Algorithm	38
4.3 Online Optical System Calibration	39
4.3.1 Estimation of Projection Matrix	39
4.3.2 Computing Optical System Parameters	42

4.4	Force Estimation	43
4.4.1	Background	43
4.4.2	Estimation Model	44
5	Experimental Results and Discussion	46
5.1	Micromanipulation Using Vision and Force	46
5.1.1	Visual Servoing Experiments	46
5.1.2	Micromanipulation Experiments	49
5.2	Parameter Estimation	51
5.2.1	Optical System Calibration Results	51
5.2.2	Online Calibration Results	54
5.2.3	Force Estimation Results	56
6	Conclusion	61
	Appendix	63
A	Derivation of the Interaction Matrix	63
	Bibliography	65

List of Figures

1.1	A Low-g Accelerometer [1]	2
1.2	A Digital Micromirror Device [2]	2
1.3	A Hard Drive's Read/Write Head [3]	2
2.1	Attractive Forces in the Micro Domain [23]	6
2.2	Micro End Effectors (a) Probe, (b) Gripper, (c) Micropipette [11]	7
2.3	Microobject Handling Strategies Using (a) Traditional Gripping, (b) Impulsive Forces, (c) Vacuum Forces, (d) Surface Tension, (e) Electrostatic Forces, (f) van der Waals Forces [23]	7
2.4	Entire Model of Workstation	8
2.5	Vision Hardware of Workstation	10
2.6	Microassembly Workstation	11
2.7	Top: (a) Eye-in-hand system. (b) Eye-to-hand system. Bottom: Opposite image motion produced by the same robot motion [30]	13
2.8	Image Based Visual Servoing Scheme	14
2.9	Position Based Visual Servoing Scheme	14
3.1	Top View of the Sample Stage	17
3.2	(a) Histogram of the Sample Stage Image, (b) Image After Thresholding	18
3.3	Segmentation Result	19
3.4	Extracted Circles	19
3.5	(a) Original Image of the Probe (b) Extracted Edge Pixels of the Probe	20
3.6	Computed Image Features for the Probe	21
3.7	(a) Defocused and (b) Focused Images	24
3.8	Results for (a) Tenengrad, (b) Energy Laplace, (c) Normed Variance	25
3.9	(a) Defocused and (b) Focused Images of a Drosophila (c) Defocused and (d) Focused Images of Pumpkin Cells	26

3.10	The Contact Force Between the Probe and the Microsphere	27
3.11	Automatic Micromanipulation of a Microsphere, (a) Initial Position, (b) Final Position	28
3.12	Obstacle Avoidance	30
4.1	Assigned Image, Objective and World Coordinate Systems	34
4.2	Calibration Patterns	38
4.3	Nonlinear Mass-Spring-Damper Model	44
5.1	Circular Path Following Task at 1X	47
5.2	Step responses and control signals at 1X	47
5.3	Step responses and control signals at 4X	47
5.4	Circular trajectory and tracking error at 1X	48
5.5	Square trajectory and tracking error at 1X	48
5.6	Square trajectory and tracking error at 1X	48
5.7	Visual Servoing in the x-z Plane	50
5.8	Automatic Micromanipulation of Microspheres	50
5.9	The Trajectory of the Corner in (a) Image and (b) World Coordinates	54
5.10	Estimated Entries of the Projection Matrix	55
5.11	(a) Prediction Error (b) Zoomed Prediction Error	55
5.12	(a) Overall Magnification Plot (b) Zoomed Magnification Plot	56
5.13	Zebrafish Embryos with Holding Gripper and Force Sensing Probe . .	57
5.14	(a) Deformation (b) Force	57
5.15	Measured and Reconstructed Force I	58
5.16	Measured and Reconstructed Force II	58
5.17	Measured and Reconstructed Force III	59
5.18	Measured and Reconstructed Force IV	60

List of Tables

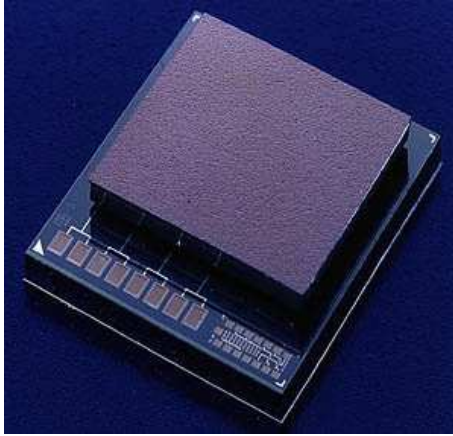
5.1	Micropositioning Accuracy and Precision	49
5.2	Trajectory Tracking Accuracy and Precision	49
5.3	Computed Calibration Parameters using Square and Circular Pat- terns for Top View	51
5.4	Computed Calibration Parameters using Virtual Patterns for Top View	52
5.5	Computed Calibration Parameters using Virtual Patterns for Side View	52
5.6	Reprojection Errors of Circular and Square Patterns for Top View . .	53
5.7	Reprojection Errors of Virtual Patterns for Top View	53
5.8	Reprojection Errors of Virtual Patterns for Side View	53

Chapter 1

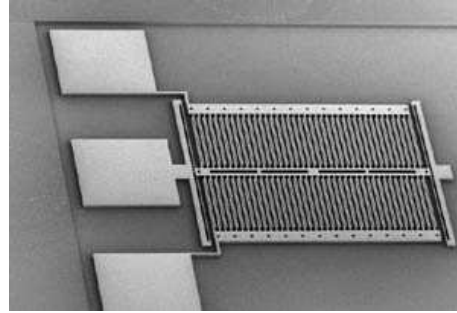
Introduction

In his famous lecture “There is plenty of the room at the bottom” in 1959, Richard Feynman considered a number of interesting ramifications on the problem of manipulating and controlling things on a small scale. In his talk Feynman described the problem of writing an enormous amount of text, the entire 24 volumes of the Encyclopedia Britannica, on a surface about the size of the head of a pin. He also discussed even more interesting possibilities to construct micromachines such as a tiny mechanical surgeon which can go into blood vessels. Although it was not possible to realize his big dream for small things at that time, he deserves the credit for recognizing the potential of miniaturization of the conventional devices that will have a major impact on society and everyday life.

With the recent advances in the fields of micro and nanotechnology, the commercial markets, including microelectromechanical system (MEMS) products such as the key components in automobile airbags (Fig. 1.1), ink-jet printers and projection display systems (Fig. 1.2), have been growing rapidly. Despite the fact that these commercially available micro devices are currently produced in a batch technique with little assembly, many other products such as read/write heads for hard disks (Fig. 1.3) and fiber optics assemblies require flexible precision assemblies [4]. However, the assembly of these products are mostly done in manual or semi-automatic operations. Furthermore, many biological micromanipulations such as invitro-fertilization, cell characterization and treatment rely on the ability of human operators. Requirement of high-precision, repeatable and financially viable operations in these tasks has given rise to the elimination of direct human involvement, and autonomy in micromanipulation and microassembly.



(a)

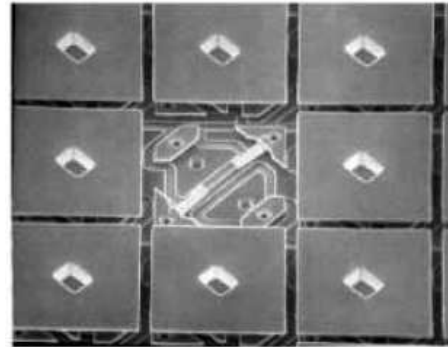


(b)

Figure 1.1: A Low-g Accelerometer [1]



(a)

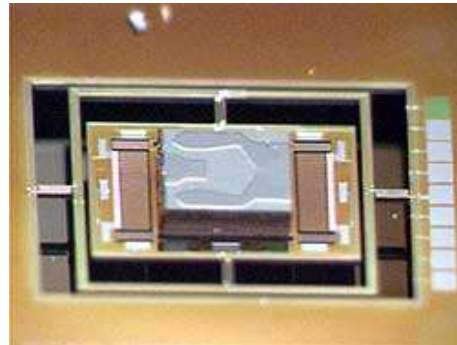


(b)

Figure 1.2: A Digital Micromirror Device [2]



(a)



(b)

Figure 1.3: A Hard Drive's Read/Write Head [3]

In the literature, several research efforts on autonomous micromanipulation and microassembly tasks under optical microscope can be found in [4]- [14]. Kim et al. [4] proposed a hybrid assembly method which combines the vision-based microassembly and the scaled teleoperated microassembly with force feedback. With these tools, 980 nm pump laser is manufactured by manipulating and assembling optoelectrical components. Beyeler et al. [7], have reported a robotic workstation consisting of a MEMS gripper and an ultrasonic manipulator. Manipulation experiments with polymer spheres, glass spheres and cancer cells are demonstrated using the ultrasonic alignment and force feedback. Wang et al [14] present a microrobotic system for fully automated zebrafish embryo injection based on computer vision and motion control. The microrobotic system performs autonomous injection at a high speed, with a successful survival rate.

Different microscope technologies such as scanning electron microscope (SEM) [24] and atomic force microscope (AFM) [16] are also preferred to monitor the manipulation process in the literature. Although these monitoring technologies ensure higher resolutions, SEM can be used only in vacuum environments for some specific particles and AFM cannot provide an online imaging during manipulation tasks. Thus optical microscope for manipulating micro particles has certain advantages including real-time imaging, reconfigurable workspace and low cost, despite the fact that small working distance and depth of field pose challenges to the three dimensional micromanipulation and microassembly.

Automated assembly of micron scale components is still an open and active research field. There exists strong demand for accurate and robust control approaches to compensate the inaccuracies in the mechanical design due to imprecise manufacturing, and to autonomously combine micro-parts from two or more different sources under non-clean room conditions. It is also desired to have more degrees of freedom for handling full 3D structures, instead of thin planar objects, with minimum user guidance and tuning.

1.1 Contributions of the Thesis

This thesis aims to develop robust and provably correct generic algorithms based on feedback provided from the imaging and force sensors which significantly enhance

our ability to observe, position, and physically transform the micro objects and contribute to applications ranging from biotechnology to MEMS. In the first part of the thesis, a robust vision control structure is designed with the real-time object and end-effector detection, optical system calibration, autofocusing and visual controller modules. Employing the developed vision based controller synthesis, the versatility and accuracy of the microassembly system is greatly improved by compensating the errors arising in open loop control. In the second part, previously designed tools combined with a motion planner in conjunction with force feedback from the end effector enable the system to achieve fully automated micromanipulation schemes which are able to achieve high accuracies using full visual feedback at each control iteration. A fully automated micromanipulation task which aims to arrange microspheres through a collision free path using vision and force feedback is successfully demonstrated to show the validity of the established algorithms. In the third part, novel estimators are developed to identify the system and to characterize the mechanical properties of the biological structures through a synthesis of concepts from the computer vision, estimation and control theory.

1.2 Outline of the Thesis

Chapter 2 introduces the concept of micromanipulation with a summary of physical effects in the microdomain. Then, an overview of the experimental setup and the fundamentals of visual servoing are given. Chapter 3 explains the vision and force subsystems for autonomously manipulating microobjects. In Chapter 4, the development of parameter estimation methods for offline and online calibration of the optical system, and characterization of the mechanical properties of a biological structure is described. Chapter 5 is on the experimental results which are implemented on the microassembly workstation. Finally Chapter 6 concludes the thesis with some remarks and gives an outlook of future works.

Chapter 2

Micromanipulation

2.1 What is Micromanipulation?

Micromanipulation is an area of microrobotics which emerged and recognized as a branch of robotics at the beginnings of 1990s. Depending on their overall size, sensing and actuation precision, part or tool size, task space, and physics being macro or microscale, robotic systems can be classified as macrorobotics or microrobotics respectively [22]. Microrobotics has two research thrust areas concerning microobject manipulation and, design and fabrication of microscale robotic agents. The first area is called micromanipulation which is defined as manipulation of objects with characteristic dimensions in the millimeter to micrometer range [23]. In a typical micromanipulation task, the size of overall system is large whereas the end effectors, manipulated objects, and sensing, actuation, and manipulation precision are demanded to be at the microscale. On the other hand, the second area focuses on miniaturization of robots down to submillimeter sizes including actuators, sensors, motion mechanisms, power sources, computing power, and wireless communication capability.

Robotic manipulation in microscale differs from the macromanipulation in many aspects. The applications of micromanipulation include manipulation of biological cells and assembly of microsized parts, thus novel tools and sensors are required to access smaller spaces. Moreover, scaling of physical effects is different and makes the object manipulation challenging in micro domain. As objects are scaled down to micrometer domain, the surface-to-volume ratio increases, surface properties and forces begin to dominate bulk or volume-based properties and forces. At this scale, inertial forces and weight are almost negligible and micro surface interatomic forces,

fluid dynamics, heat transfer, surface chemistry, and adhesion based forces dominate the robot mechanics. In other words, nevertheless the same physical laws govern the microscopic world as the macroscopic world, the relative importance of them are changed [23].

In order to visualize the effect of scaling, a simple task to lift an object using a tool with electrostatic, magnetic and van der Waals forces is designed. The attractive forces are given in terms of ratio between the resulting interaction forces and the weight of the object in Fig. 2.1. For the magnetic interaction, it is assumed that two permanent magnets are aligned along their magnetization, while in the electrostatic case, the tool is assumed to behave as an infinite halfspace. To compute the magnetic force, the tool is considered to be cylindrical with radius $4r$ and height $8r$, where r is the radius of the sphere. In both the magnetic and electrostatic cases, the distance between the tool and the sphere is assumed to be αr , where α is a positive scalar. It is observed that gravity is the dominant force for $r > 1$ m, while the magnetic force is sufficient to lift the sphere. For $r < 10^{-4}$ m the electrostatic force dominates over gravity. In addition, the van der Waals force governs the interaction for $r < 10^{-7}$ m.

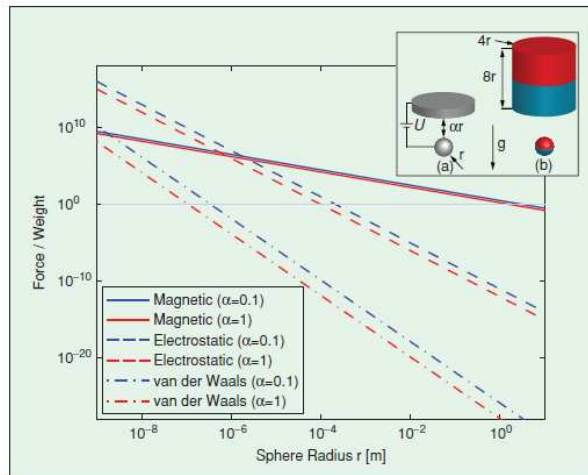


Figure 2.1: Attractive Forces in the Micro Domain [23]

Depending on the dominant forces and the functional requirements at the micro, specific actuators, grippers and sensors are demanded in manipulation tasks. In typical micromanipulation systems, single-axis and multi-axis micromanipulators with a travel range of a few millimeters and a resolution better than $1 \mu\text{m}$ are preferred.

Dc motors, stepper motors, or piezo drives are characteristically used to drive the positioning stages. In addition to the stages, micromanipulation tasks require specific end effectors such as probes, micropipettes, or microgrippers to access to small spaces, shown in Fig. 2.2. Exploiting the dominant forces at microscale, several potential object handling types are shown in Fig. 2.3.

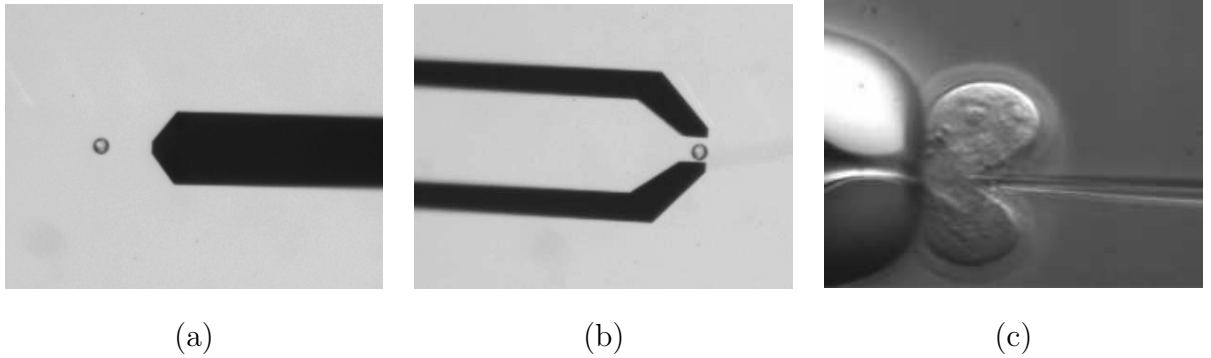


Figure 2.2: Micro End Effectors (a) Probe, (b) Gripper, (c) Micropipette [11]

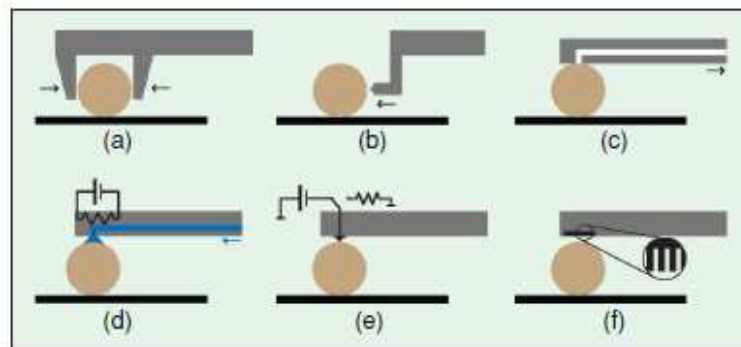


Figure 2.3: Microobject Handling Strategies Using (a) Traditional Gripping, (b) Impulsive Forces, (c) Vacuum Forces, (d) Surface Tension, (e) Electrostatic Forces, (f) van der Waals Forces [23]

Besides the positioning stages and end effectors, an important issue in micromanipulation concerns the measurement and control of the forces. The involved force magnitudes typically vary between 10^{-3} to 10^{-6} N and below in the micro domain. Thus, novel force sensors with high resolution and accuracy are also required to use force sensors to measure and to characterize the manipulation forces in microscale. To satisfy these requirements, force measurements in micro domain are usually done by measuring the change in certain properties of the sensing elements such as strain gauges, piezoelectric, capacitive sensors or using laser-based optical techniques such

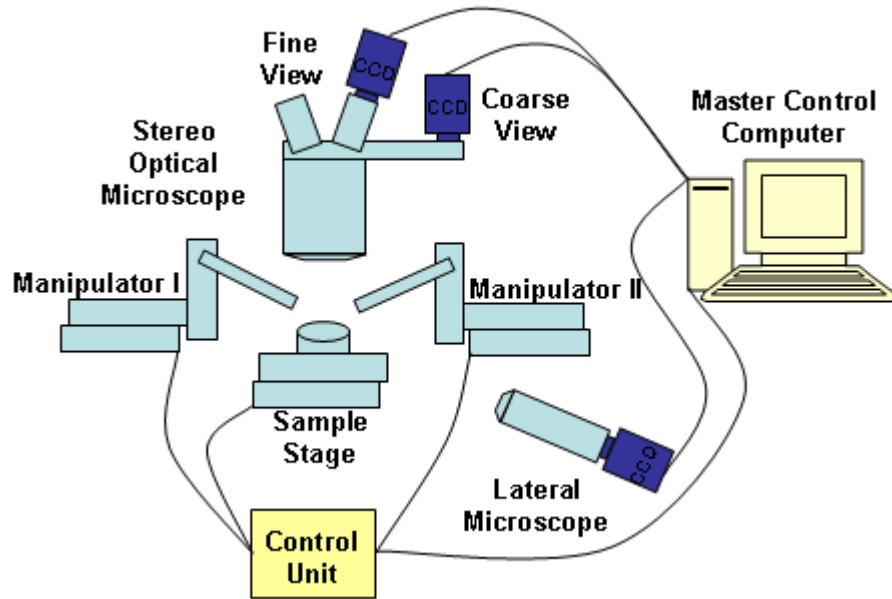


Figure 2.4: Entire Model of Workstation

as atomic force microscope [20].

2.2 Microassembly Workstation

In the microworld, there exists certain uncertainties about the position, behavior and shape of the objects to be manipulated. Parts may stick, flip away and deformed with an applied force in micromanipulation tasks. In addition, the shapes of micron sized objects may not agree with the designed geometry, since manufacturing systems cannot ensure very high precisions in μm . Therefore, a microassembly workstation was developed to compensate the mentioned uncertainties and to manipulate small parts with small tolerances and at high accuracies. The model of the overall experimental system setup is shown in Fig. 2.4.

The mentioned functional requirements for the microassembly workstation call for the use of external sensors to guide manipulation tasks. Thus, three types of feedback are provided from the vision, position and force sensors in the system. The vision system constitutes the key component in the setup, since high precision micromanipulation is strongly dependent on the visual feedback which allows direct measurement of positions and orientations of the objects and the end effectors. A visually guided manipulation implies the use of monitoring devices with high magnifications such as microscopes. Based on the specifications of a micromanipulation

scenario, the size of the object to be manipulated and thus the required resolution and field of view may vary. Before the properties of the vision system are presented, some basic definitions about optical microscopy should be reviewed.

- Magnification is the ratio between distance between two points on a specimen and their corresponding projections in an image under the assumption that these points lie on a surface parallel to the image plane.
- Field of view is the maximum visible area that can be monitored by the optical system. High magnifications imply narrower field of view. Thus, using multiple vision sensors at different magnifications, we can provide to monitor a relatively large field with better resolution.
- Depth of field is the distance between the closest and farthest objects in focus within a scene as viewed by a lens at a given focus. The manipulators and objects must move within the depth of field to be monitored and tracked at each iteration. Due to the small depth of field in optical microscopes, it is challenging to realize 3D manipulation tasks under an optical microscope.
- Working distance is the distance between the closest surface of the monitored object and the objective front lens. It must be large to allow unobstructed motions of the manipulators.

In the microassembly workstation different magnification and resolution levels are available. In order to allow global and local visual information, a coarse and a fine view with variable zooming are employed. These cameras are mounted on a stereo optical microscope, Nikon SMZ1500 with 1.5x objective and 0.75:11.25 zoom ratio. While an A602fc Basler with $9.9 \times 9.9 \mu\text{m}$ cell sizes provides coarse view for the sample stage, a Sony XCD-X710CR with $4.7 \times 4.7 \mu\text{m}$ cell sizes is used for fine and narrower field of view. The vision system is shown in Fig. 2.5.(a).

A typical visually guided manipulation requires the position information of the object and the end effector in x, y and z to realize 3D manipulation tasks. However, it is challenging to get the measurement in z axis for a micromanipulation task, since optical microscopes suffer from the low depth of field which limits the focal plane into a small range and causes defocused view of the object monitored outside this

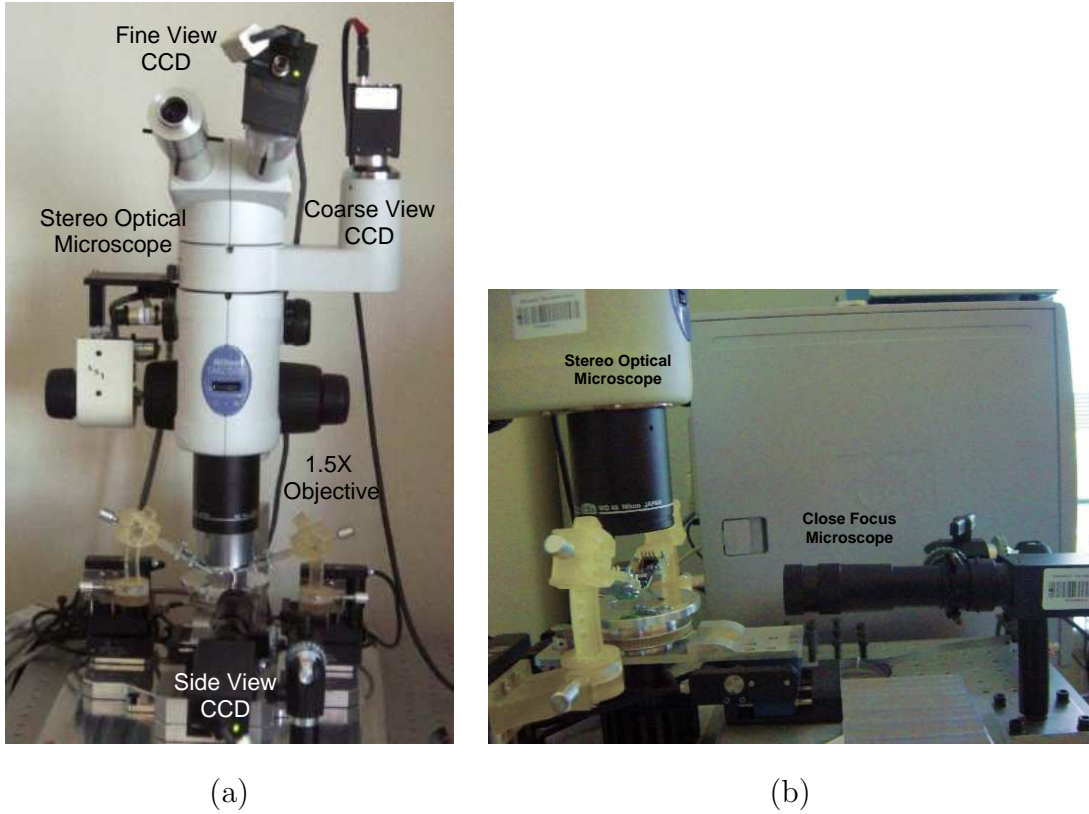
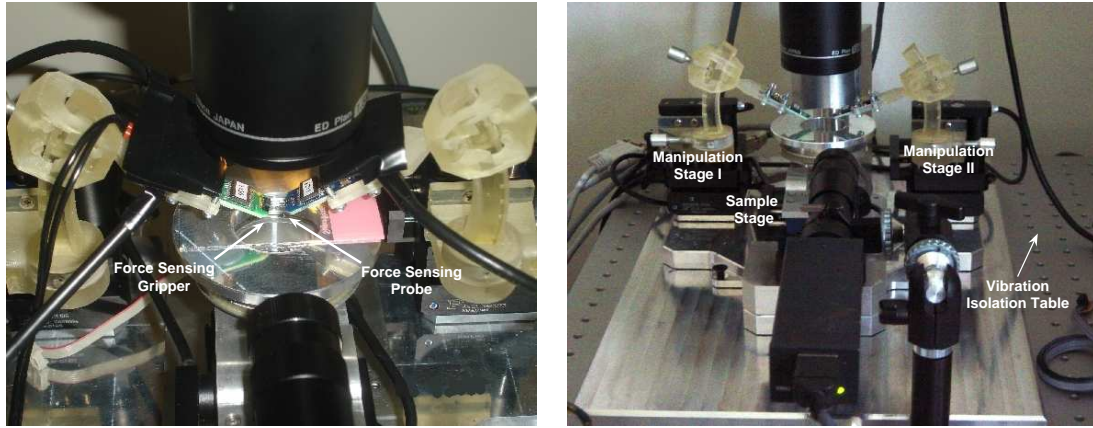


Figure 2.5: Vision Hardware of Workstation

region. Although exploiting defocus can yield a coarse information along the z axes, it results in poor accuracy for micron precision applications and it is computationally expensive. Thus, to acquire the height information for the interested object, a lateral microscope with an additional CCD camera is employed. A Sony XCD-X710CR coupled to a 35x close focus microscope with variable zoom and relatively long working distance is used to acquire the height information between the sample stage and the end effector, shown in Fig. 2.5.(b).

It is also important to accurately handle the micro parts for a dexterous manipulation, since the micro parts to be manipulated are usually fragile. Therefore two types of end effectors, a probe and a microgripper which are integrated with capacitive force sensors and are able to sense the forces down to $0.4 \mu N$ and $0.01 \mu N$ respectively. The force sensing probe and gripper are mounted on tilted holders to reach the desired point effectively. An illustrative figure is given in Fig. 2.6.(a). The inclined end effectors can approach to micro samples without touching undesired points on the sample stage. However, the inclination leads to the requirement of relatively large working distance and depth of field. Therefore a 1.5x objective



(a) End Effectors

(b) Sample and Manipulator Stages

Figure 2.6: Microassembly Workstation

with 44.5 mm working distance is utilized to provide well focused images of the end effectors and samples.

Transporting and positioning the microparts are crucial for the execution of the microassembly tasks as well as the handling issues. The force sensing probe and gripper are mounted on two separate 3-DOF fine positioning stages (PI M111.1DG with effective x-y-z range of 15x15x15 mm and 50 nm closed loop precision). On an x-y- θ positioning stage, (PI M111.1DG with effective x-y range of 15x15 mm, 50 nm close loop precision, and 4.5×10^{-5} degrees rotation resolution) a glass slide is mounted and is positioned under the force sensing probe and microgripper. On the glass slide, the samples, polystyrene balls and biological cells which are used in experiments can be located. The high precision positioning stages are depicted in Fig. 2.6.(b).

The system consists of three IEE1394 cameras, 9 DC motors and an illumination system. All those components are controlled with a centralized structure including a main and a slave control computer. While the main control computer gives reference values without any direct connections to the actuators, force and positioning sensors, the slave one runs a fast control loop based on the directives from the main computer. The control software is written in the C programming environment and provides real-time control for moving and positioning the stages precisely. Moreover, video data from the IEE1394 cameras is directly transferred to the main computer and the computer vision software is written in C++ environment by using the OpenCV library.

2.3 Visual Servoing

The majority of the industrial robots operate in certain workplaces which are designed to suit the robots. In today's world, robots are not fully capable of working in uncluttered environments due to the limitations in their sensory information and data processing capability. Although it has already been known that enhancing the number and output quality of sensors improves the versatility and flexibility of the commercial robots, it has not been proved to be cost-effective yet.

The development of digital camera and microprocessor technology in the early 1990's enables to use low-cost and high performance vision units in robotic applications. Nevertheless vision is not prevalently used in factories yet, using visual information has become one of the effective way to compensate the uncertainties in the calibration of systems, manipulators and workspaces in some fields such as micromanipulation and microassembly. In the micro domain, high precision relies on an accurate calibration of the system. However, strictly depending on the model of the systems suffers from the thermal growth errors that can only be compensated using large and expensive cooling systems [6]. Moreover, it is more difficult to model the mentioned forces in micro domain. Thus, visual servoing methods are employed to compensate the modeling uncertainties for cost effective and reliable manipulations in this setup.

Visual servo control refers to using visual feedback to control a robot. The visual information may be obtained from a camera that is mounted on a robot and moving with the robot or the camera can be stationary and observe the robot motion from a fixed point. These two configurations are called eye-in-hand and eye-to-hand systems respectively. An illustrative figure is shown in Fig. 2.7. In addition, different configurations such as multiple cameras on pan-tilt heads observing the robot motion also exist in the literature.

Visual servoing has been extensively studied in various forms for more than three decades starting from simple pick-and-place tasks to today's real-time, advanced manipulation of objects. Over the past years, intense research effort in this area has resulted in numerous visual servoing approaches. In 1980 visual servo systems were classified into two groups in terms of their control structure by Sanderson and Weiss [26]. In the first group, control of the robot is performed in two

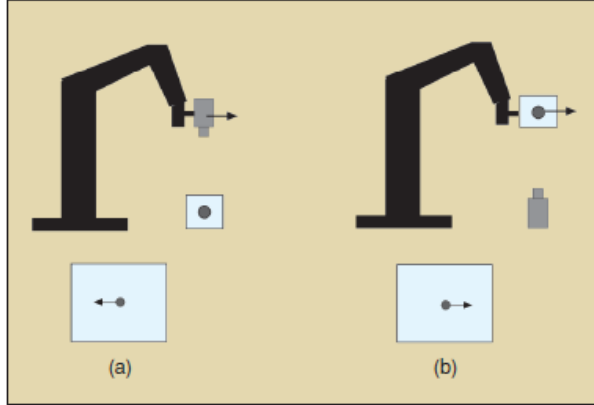


Figure 2.7: Top: (a) Eye-in-hand system. (b) Eye-to-hand system. Bottom: Opposite image motion produced by the same robot motion [30]

stages. Vision controller transmits the input to robot controller and it converts the signal into joint feedback. This group is called dynamic-look-and-move systems. In the second group, the vision controller directly sends the control input to the joints which is called direct visual servoing [29]. Another taxonomy classifies the visual servo schemes into two main groups, image-based visual servoing (IBVS) and position-based visual servoing (PBVS) [27], [28]. In IBVS, two dimensional image measurements are used directly to estimate the desired movement of the robot. The second approach is based on computation of camera pose from a set of measurements which requires a calibrated camera and the 3D model of the observed object. IBVS and PBVS structures are schematically shown in Fig. 2.8 and Fig. 2.9 respectively. In the figures, the joint inputs and the visual control laws are denoted by \dot{q} and v respectively. From the figures, one can observe that visual servo control relies on techniques from image processing, estimation and control theory. The basic components of the IBVS scheme, feature extraction, real-time tracking and visual control law design are explained in the next chapter.

Formally speaking, a typical vision based control scheme can be formulated as follows. The error function $e(t)$ for a conventional visual servoing method can be given by

$$e(t) = s(m(t), a) - s^* \quad (2.1)$$

where $m(t)$ denotes a set of image measurements (e.g., corner, object centroid) and a contains an additional information about the system such as the intrinsic parameters

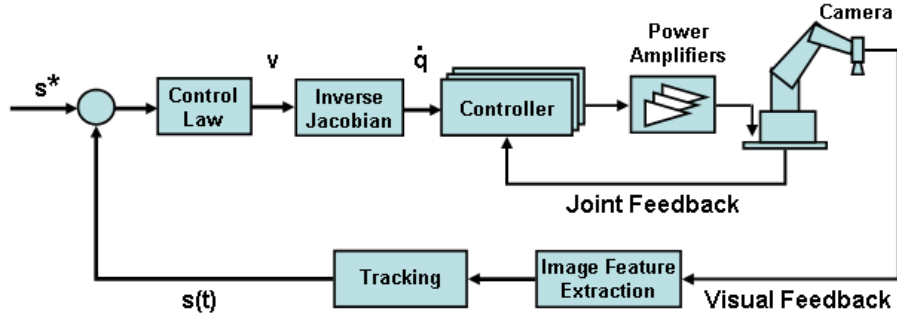


Figure 2.8: Image Based Visual Servoing Scheme

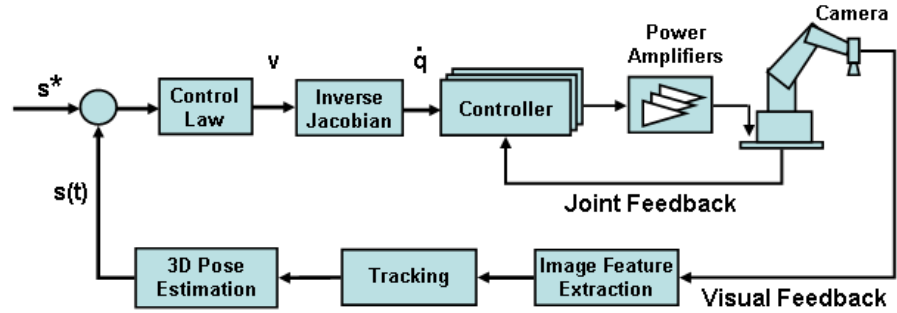


Figure 2.9: Position Based Visual Servoing Scheme

of the camera or 3D model of the object. These terms are used to compute a vector of k visual features, $s(m(t), a)$. s^* contains the desired values of these features. According to the previously stated taxonomy, IBVS and PBVS differ how we design the vector s . In IBVS, s contains a set of features which are already available in the image. In PBVS, s consists of a set of 3-D parameters, which has to be computed from image measurements.

Having selected the way how to design the vector s , a velocity control law can be easily designed by exploiting the relationship between s and the spatial velocity of end effector in the camera frame. Let the kinematic screw is denoted by $(\mathbf{v} = (v, \omega)^T)$ with the instantaneous linear velocity v of a point in the space and the instantaneous angular velocity ω of the end effector frame.

The relationship between s and \mathbf{v} is given by

$$\dot{s}(p, t) = \frac{\partial s}{\partial p} \frac{dp}{dt} + \frac{\partial s}{\partial t} = L_s \mathbf{v} + \frac{\partial s}{\partial t} \quad (2.2)$$

where p is the pose between the camera and the end effector, k is the number of the image features, v is the difference between the end effector and the camera velocity,

$L_s \in R^{k \times 6}$ is the image interaction matrix which is a function of the visual features and intrinsic/extrinsic parameters of the visual sensor.

Having (2.1) and (2.2), the relationship between the time variation of the error and the end effector velocity is given

$$\dot{e} = \dot{s} - \dot{s}^* = L_e \mathbf{v} + \frac{\partial e}{\partial t} - \frac{ds^*}{dt} \quad (2.3)$$

where $L_e = L_s$ and $\frac{\partial e}{\partial t}$ is the time variation of e .

Considering \mathbf{v} as the input to the robot controller, numerous solutions are proposed to regulate the task function (2.3) such as P, PI, PID [27], nonlinear control law [31], optimal control [32], predictive control [33], robust control [34] and invariant visual servoing [35].

Chapter 3

Micromanipulation Using Vision & Force

In the literature, several micromanipulation works are presented with no sensor [19], only visual feedback [17], [18] and both vision and force information [4], [10], [15]. Since manipulating an object needs the ability to observe, position, and physically transform the object, both vision and force are essential feedback types for our versatile micro-assembly system. In this chapter, we are presenting the end-effector and object detection, real-time tracking, visual controller synthesis, autofocus methods, force feedback and path planning algorithm.

3.1 Visual Feedback

3.1.1 Object and End Effector Detection

Manipulating micro objects with the probe/gripper requires the knowledge of position of the probe/gripper and the object. In order to obtain these information, we need to have a priori information about the size and shape of the probe/gripper and the object. In the micromanipulation experiments, micro polystyrene balls with different diameters (between 8 and 70 microns) are manipulated by the probe which is mounted on the x-y-z positioning stage. In each experiment, only one type of polystyrene balls with same diameter size is used. Thus, we can use this a priori knowledge on the geometrical models of the objects and the probe in the detection algorithms.

Having characterized the geometrical properties of the objects and the probe, it is important which information has to be extracted from the image. Center of gravity of an object, corner point, area of a surface and distance between two points can be given as examples to the image features. In the experiments, it is aimed to push

the microobjects to the desired locations accurately using a probe. To facilitate such a scenario, we need to have the information about the center of gravity of the microball, its diameter, the tip location and orientation of the probe. Thus, several image processing algorithms, using a priori size and shape information, are developed to obtain the desired features in the setup.

Object Detection

Since the probe moves in the three dimensional space, it is vital to detect the three dimensional coordinates of the contact point on the ball. Thus, real-time extraction of that point from the top and side cameras becomes crucial. Since the top and side views can be assumed to be calibrated, the same algorithm is implemented for the images from the cameras. Since the cameras have different configurations and have been exposed to different illumination effects, different thresholding values are assigned for the two views.

The first step in the circle detection algorithm aims to remove the noise and the perturbations by using a smoothing filter. An illustrative top view of the workcell which contains several microballs and some dust particles is shown in Fig. 3.1. One can observe that back-lighting is used to illuminate the sample stage, since the

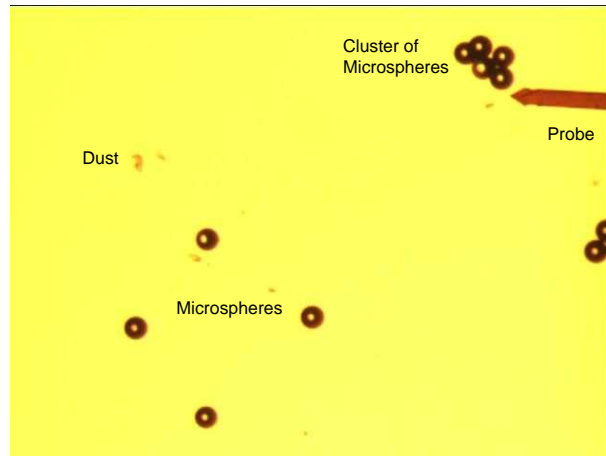


Figure 3.1: Top View of the Sample Stage

illumination from above makes the image processing harder and unstable due to the reflectance from the shiny surface of the polystyrene balls.

The next step is to differentiate the balls from the background. Since the back-light illumination power is controllable, a threshold is automatically set by using the

90 percent of background intensity value. It can be observed from the Fig. 3.2.(a), the large number of pixels gathered around the intensity value 235 which is the mean background grayscale value. The thresholded image is depicted in Fig. 3.2.(b).

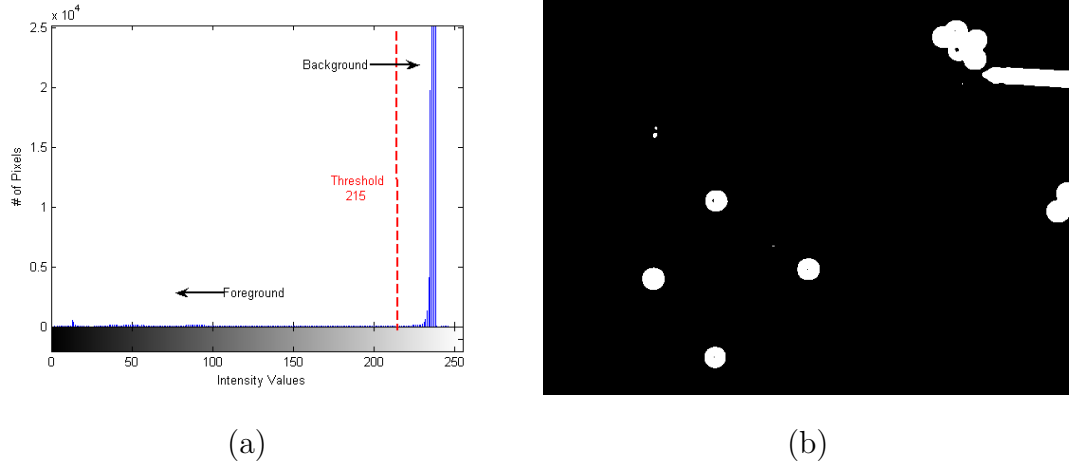


Figure 3.2: (a) Histogram of the Sample Stage Image, (b) Image After Thresholding

In the next step, a connected component finder algorithm is employed to retrieve all the contours and organizes them into two-level hierarchy for the thresholded image in the previous step. As the connected components are found, the contours whose areas are in the predetermined range are chosen as the region of interests. Now we can eliminate the regions where the clusters of microballs and relatively bigger dust from the microspheres standing alone. Note that the cluster of balls are not chosen to be manipulated due to difficulty in separation. The resulting segmentation yields the regions which contains only the individual microspheres, depicted in Fig. 3.3. Having the balls segmented, the generalized Hough transform which is robust under noise is implemented to detect the spheres, shown in Fig. 3.4. It should be notified that the Hough transform with a minimum distance criteria between the centers might be employed to detect the circles in the entire frame without using the previous steps. However, it would not allow a real-time performance. On the other hand, using the explained algorithm, the center positions and radii of the spheres are detected at a rate of 60 Hz in the experiments.

End Effector Detection

It is vital to detect and update position of the end effector from the top and side cameras during the experiments in order to increase manipulation precision. Since

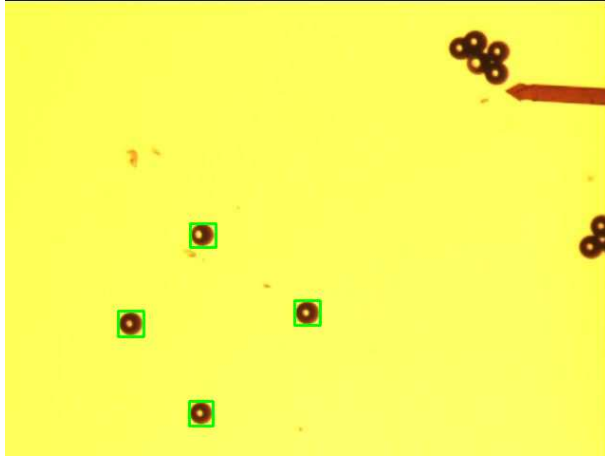


Figure 3.3: Segmentation Result

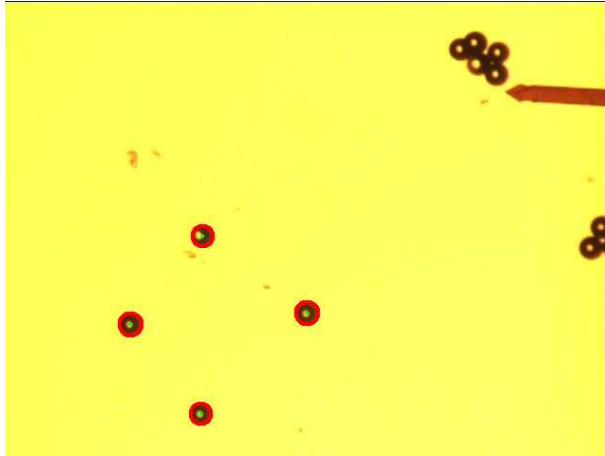


Figure 3.4: Extracted Circles

the end effector is moved in the 3D, two individual algorithms are required to detect the position of the probe in the x-z and x-y plane.

The geometries of the end-effector in the x-y and x-z planes which can be measured with the two microscopes (optical and close focus) are constant. It is well known that template matching methods give good results for this sort of detection problems. Template matching compares for the best match with a reference template by sliding the template from the top left to the bottom right of the image. One of the drawbacks of template matching is its large computational cost. The size of the template and image are the factors that determine the computation time. However, the template size is also important for the robustness of detection. Thus, an optimal size of image with a region of interest and template is chosen in the experiments. Another shortcoming is that template matching does not give subpixel

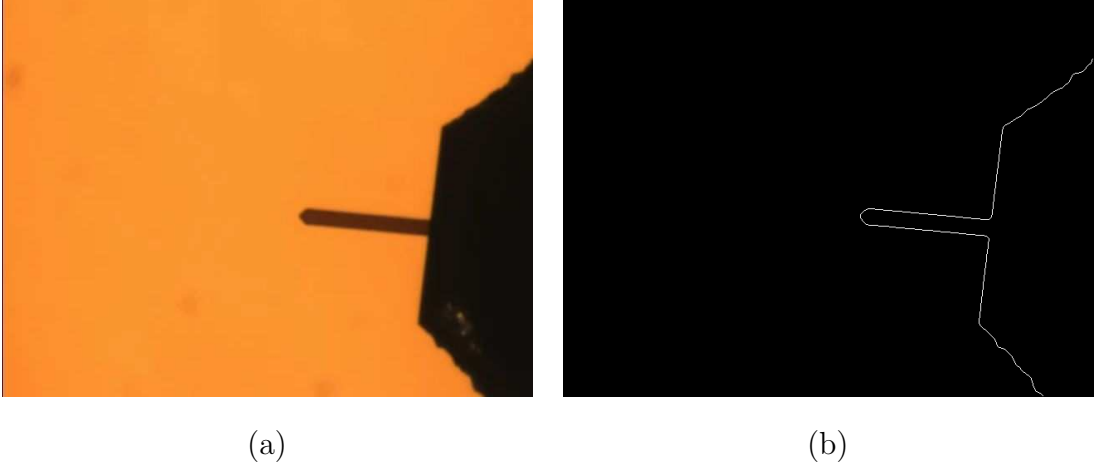


Figure 3.5: (a) Original Image of the Probe (b) Extracted Edge Pixels of the Probe

results, unless it is modified with an interpolation algorithm. Since it is not required to have subpixel accuracy in the x-z plane (side camera), the probe is detected by using template matching with the Normalized Cross Correlation (NCC) technique comparison method,

$$C(u, v) = \frac{\sum_{x,y} (I(u+x, v+y) - \bar{I}_{u,v}) T(x, y)}{\sum_{x,y} (I(u+x, v+y) - \bar{I}_{u,v})^2 \sum_{x,y} T(x, y)^2} \quad (3.1)$$

where $I(u, v)$, $T(x, y)$ and $\bar{I}(u, v)$ denote the image, template and local image mean at location (u, v) respectively. The brightness of the image and template can vary due to lighting conditions during the experiments. Thus NCC method which uses the normalized images is employed to eliminate the illumination effects.

Computing the contact point of the probe in the x-y plane is vital to locate microspheres to the desired targets precisely. Therefore the detection of probe tip is computed in subpixel accuracy by exploiting the known geometry of the probe. In the algorithm, the edge points of the probe are extracted by the Canny edge detector. The original image and edge map of the probe are shown in Fig. 3.5. Since we have a priori information about the geometry and the orientation of the probe, the edge pixels with the predetermined slopes can be fitted to two parallel lines in a subpixel accuracy. It is assumed that the probe tip is on the line which is parallel and in the middle of the previously extracted lines. The exact coordinate of the tip is computed through searching the first edge pixel along the line. The detection algorithm is illustrated in Fig. 3.6. Note that in the presented detection algorithms in x-y and x-z planes, it is assumed that the home position of the probe

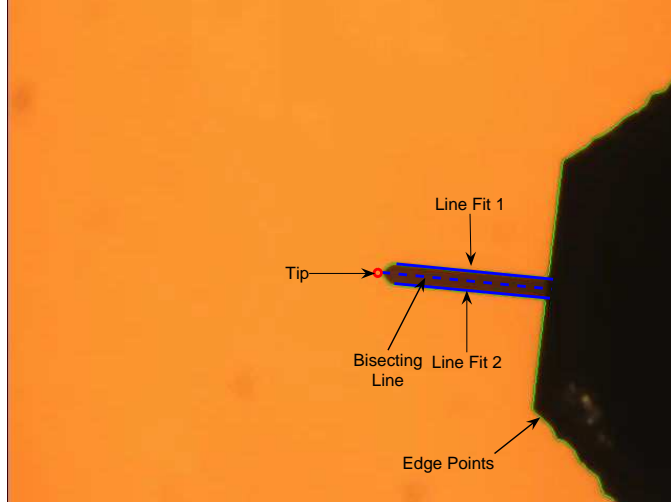


Figure 3.6: Computed Image Features for the Probe

is known.

3.1.2 Real-Time Tracking

After the initial detection of the object and the probe, it is not required to process the entire image for the following frames. Having computed the required image features of object (x_{k-1}^{obj}) and the probe tip (x_{k-1}^{tip}) for $t = k - 1$, the positions can be estimated using an estimator for the next time step $t = k$. Assuming that the motions of the object and the probe are governed by the linear difference equations,

$$x_k = Ax_{k-1} + Bu_{k-1} + w_{k-1} \quad (3.2)$$

with a measurement $z \in \mathfrak{R}^m$

$$z_k = Hx_k + v_k \quad (3.3)$$

where $x_k \in \mathfrak{R}^n$ is the state vector and $A \in \mathfrak{R}^{n \times n}$ is the state transition matrix. The matrix $B \in \mathfrak{R}^{n \times l}$ relates the optional control input $u \in \mathfrak{R}^l$ to the state x_k . The matrix $H \in \mathfrak{R}^{m \times n}$ relates the state x_k to the measurement z_k . The random variables w_{k-1} and v_k represent the white process and measurement noise with normal probability distributions respectively.

Based on the model in (3.2) and (3.3), the estimated object center \hat{x}_k^{obj} and the probe tip \hat{x}_k^{tip} can be computed using the discrete Kalman filter [40]. Once we have \hat{x}_k^{obj} and \hat{x}_k^{tip} , these coordinates can be used to define new regions of interest at $t = k$ in which the detection is performed. Employing a region of interest improves

the computation time and robustness of the mentioned detection algorithms. As a result, the locations of two image features, position of the probe tip and the sphere which is being pushed are tracked by the tracking module in real-time during the micromanipulation experiments.

3.1.3 Visual Control Law

The complex geometry of the observed biological samples and high numerical apertures of optical microscope, which results in small depth of field, lead to a challenging 3D pose estimation problem. Therefore, an image based visual servoing approach is preferred in the micromanipulation tasks. In addition, eye-to-hand configuration is assumed in the vision based control design, since the vision sensors are stationary in the setup. Thus, considering \mathbf{v} as the input to the robot controller in the equation (2.2), a simple proportional control to ensure an exponential decoupled decrease of the error ($\dot{e} = -\lambda e$) is designed:

$$\mathbf{v} = -\lambda L_s^\dagger e \quad (3.4)$$

where λ is a scalar and $L_s^\dagger \in \mathbb{R}^{6 \times k}$ is the pseudo inverse of L_s matrix. Note that the derivation of the interaction matrix for a point feature is given in the Appendix A.

It is also possible to design control laws that optimize various system performance measures.

Optimal Visual Controller Synthesis

Equation (2.2) can be written in discrete time as

$$s(k+1) = s(k) + TL_s(k)\mathbf{v}(k) \quad (3.5)$$

where $s \in \mathbb{R}^{2N}$ is the vector of image features being tracked, N is the number of the features, T is the sampling time of the vision sensor, and $\mathbf{v}(k)$ is the velocity vector of the end effector.

Employing the optimal control techniques in [32], the cost function can be redefined to penalize the pixelized position errors and the control energy as

$$E(k+1) = (s(k+1) - s^*(k+1))^T Q (s(k+1) - s^*(k+1)) + \mathbf{v}^T(k) L \mathbf{v}(k) \quad (3.6)$$

The resulting optimal control input $\mathbf{v}(k)$ which minimizes the cost function can be derived as

$$\mathbf{v}(k) = -(TJ^T(k)QTJ(k) + L)^{-1}TJ^T(k)Q(s(k) - s^*(k+1)) \quad (3.7)$$

The weighting matrices Q and L can be adjusted to ensure desired response.

3.1.4 Autofocusing

It is challenging to use visual feedback in microassembly due to the small depth of field in microscopes. When we use microobjects with different heights, inclined surfaces or cameras whose optical axis are not perpendicular to the scene, only small portions of the workspace might be in focus. However, object detection algorithms often demand sharply focused images to obtain the certain information. Thus, it is important to capture focused images of a moving image feature such as tip of an end effector in the 3D space during a microassembly task. In order to use the visual feedback efficiently in the experiments, we developed an autofocusing module to continuously have sharp images of the features tracked.

According to Krotkov [36], the first problem of automatic focusing is that given the projection $P' = (u, v)$ onto the focal plane of an object point $P = (x, y, z)$ (z unknown), what focal length, produces the sharpest definition of P' ; and the second problem is given the focal length acquired from autofocusing, to recover the z component of P which is the depth. Our main consideration in the experiments is the first one.

In the literature, a variety of algorithms to measure the sharpness of an image are proposed and compared [36], [37]. These methods can be classified into three main groups: derivative, statistics and histogram based methods. The derivative based methods relate the focus measure with the high frequency content in the images. The second group searches for focused images using correlation and/or variance. The third, one focus measure is determined by exploiting the histogram of spatial and frequency intensities in the image. In order to judge the performance of the focus measures for the manipulation experiments, the best three criterions, two derivative based (Tenengrad and energy laplace) and a statistics (normed variance) based methods are evaluated. The focus criterion functions for the measures are

given as

$$\begin{aligned}
F_{Tenengrad} &= \sum_{Width} \sum_{Height} I_x^2(u, v) + I_y^2(u, v) \\
F_{energylaplace} &= \sum_{Width} \sum_{Height} C(u, v) \\
F_{normedvariance} &= \frac{1}{Height \times Width \times \mu} \sum_{Width} \sum_{Height} (I(u, v) - \mu)^2
\end{aligned} \tag{3.8}$$

where I_x and I_y are the derivatives of the image I along x and y directions respectively. $C(u, v)$ is the second derivative of I image and μ is the mean of the intensities in I .

In order to test the algorithms, a sequence of the images at different Z coordinates are captured. Since all the regions in the field of view do not have the same height, a planar patch on the captured object using 50×50 pixels window are chosen to be processed during the experiment. The microscope moves along the z axis in a range of 1750 microns with 5 micron steps. In order to eliminate the displacement of the object in x and y directions due to the tilt angles between the camera and the sample frame during the z movement, the center of the monitored object is aligned with the image center. The positioning stages are driven to minimize the distance between the image and object center using the visual feedback. Figure 3.7 shows two aligned images of a resistance with the dimensions $2 \times 1 \times 0.5$ mm from the captured array at different depths.

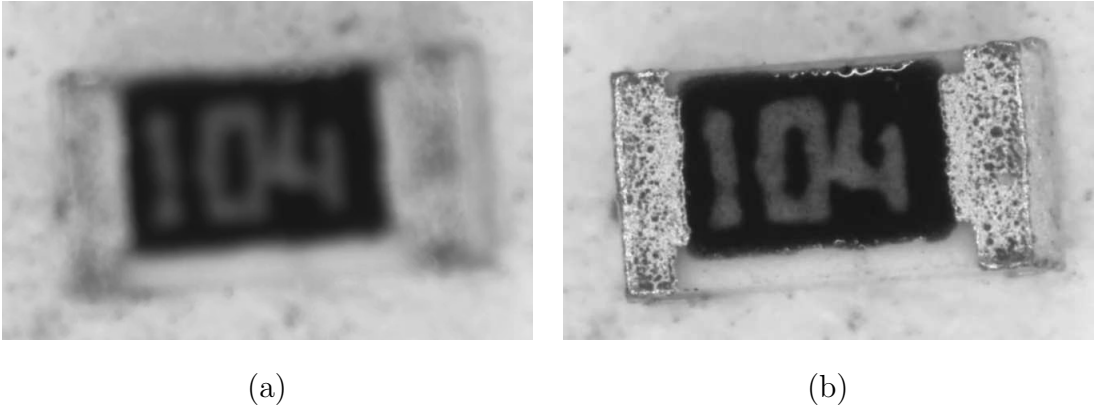
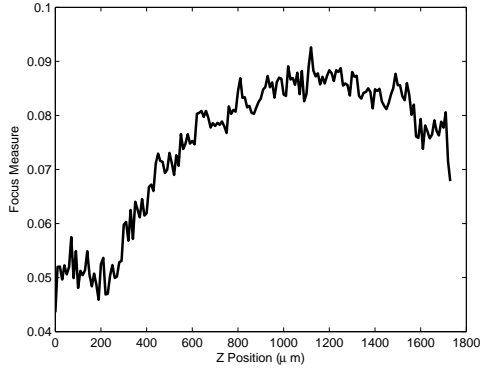


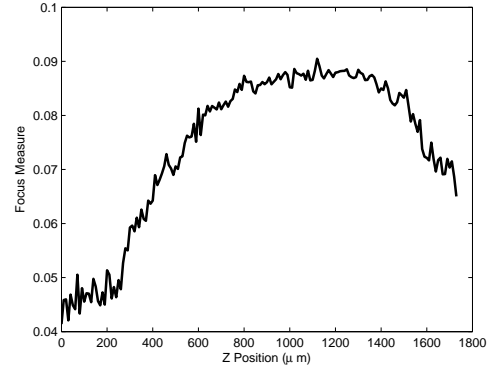
Figure 3.7: (a) Defocused and (b) Focused Images

The results of the presented focus measures are depicted in Fig. 3.8. Note that in order to make valid comparisons, the focus curves are normalized.

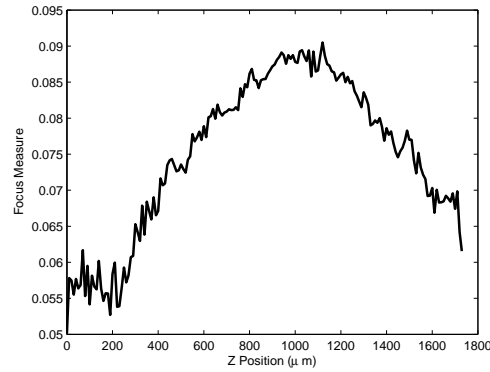
Before evaluating the results, it should be known that creating an image sequence with small linear incremental steps is a very slow process. Thus, the optimal focus



(a)



(b)



(c)

Figure 3.8: Results for (a) Tenengrad, (b) Energy Laplace, (c) Normed Variance

measure should be unimodal, monotonic, and should reach the maximum only when the image is focused in order to support a faster algorithm [38]. According to this criterion, the statistics based algorithm, the normalized variance performs better performance than the other two algorithms. It is more selective to the focus changes and has less local maximums. Although this algorithm amplifies the effect of noise, the images can be pre-processed before the focus measure.

Based on the unimodal assumption of the focus measure profile, the normalized variance focus measure was applied using Fibonacci Search, a technique to narrow the parameter space down to the peak sharpness in the mentioned z -axis range for the focusing motor. In the application of this technique, an interval in the z -axis is chosen i.e. $[a, b]$. Then, in this interval, two z -axis values a_1 and b_1 are chosen, where $a_1 < b_1$ using Fibonacci numbers. At a_1 and b_1 , the sharpness is calculated according to the normalized variance focus measure. Finally, if sharpness at a_1 is bigger, the new interval is $[a, a_1]$, else the new interval is $[b_1, b]$. The search algorithm

works that way and at each step, the interval where the highest sharpness will be searched becomes smaller. As a result, the algorithm finds at which depth the highest sharpness occurs and acquires the sharpest image. The initial and focused images of two samples using the presented algorithm are depicted in Fig.3.9.

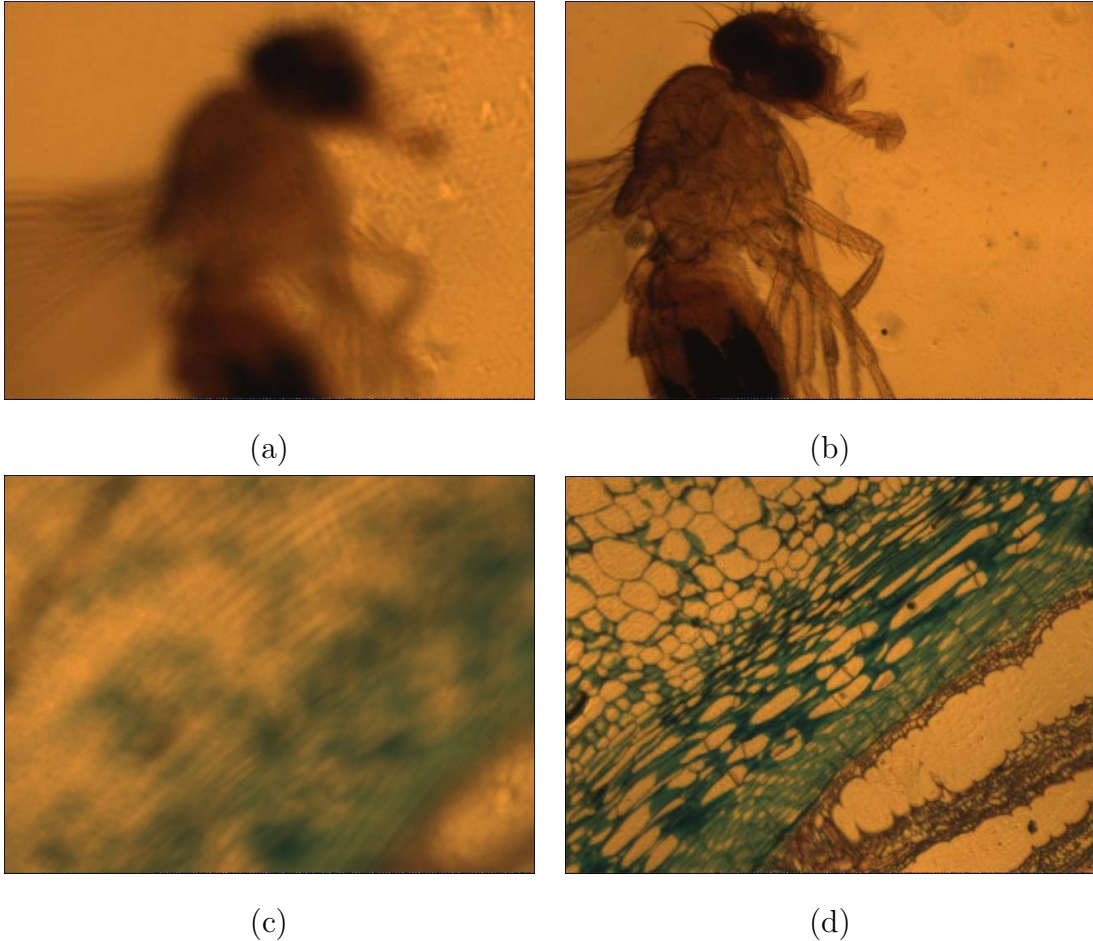


Figure 3.9: (a) Defocused and (b) Focused Images of a Drosophila (c) Defocused and (d) Focused Images of Pumpkin Cells

3.2 Force Feedback

Visual information without force feedback is not adequate for sophisticated micro-manipulation tasks which requires a high degree of dexterity. Using only visual data, we can model and control positioning of an object. However, pure position control for delicate or fragile objects such as biological material cannot ensure safe and successful manipulation strategies. Thus, force control is required to manipulate the objects successfully without damaging to the object. Furthermore, force

feedback in the micromanipulation tasks can also be used to detect the interaction forces between the end effector and the object. This information is employed to reconstruct the state of the objects and to characterize the mechanical properties of the object by the authors of [13], [14].

In our setup, the end effectors, the probe and the gripper, are equipped with capacitive force sensors which can sense compression and tension. In the micromanipulation tasks, we are able to continuously sense the interaction forces during a contact between the object and the probe. This information can be used to control the manipulation force in order to prevent excessive forces that may damage the probe and the object, and push the object to undesired locations. An example plot which demonstrates the interaction force between the microsphere and the force sensing probe is given in Fig. 3.10.

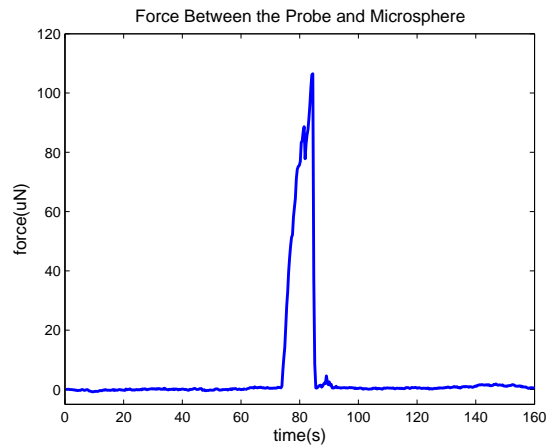


Figure 3.10: The Contact Force Between the Probe and the Microsphere

3.3 Path Planning for Collision-Free Transportation of Microobjects

In the previous sections, we explore the required modules to dexterously manipulate the microparticles. Using the object detection, tracking, visual and force control modules, we are able to construct an algorithm to push a microsphere along a designed path and locate it to the desired target. An illustrative scene for the problem task is given in Fig. 5.8.

The stated micromanipulation task for a microsphere can be extended to the scenarios which aim to move several microparticles serially along the computed

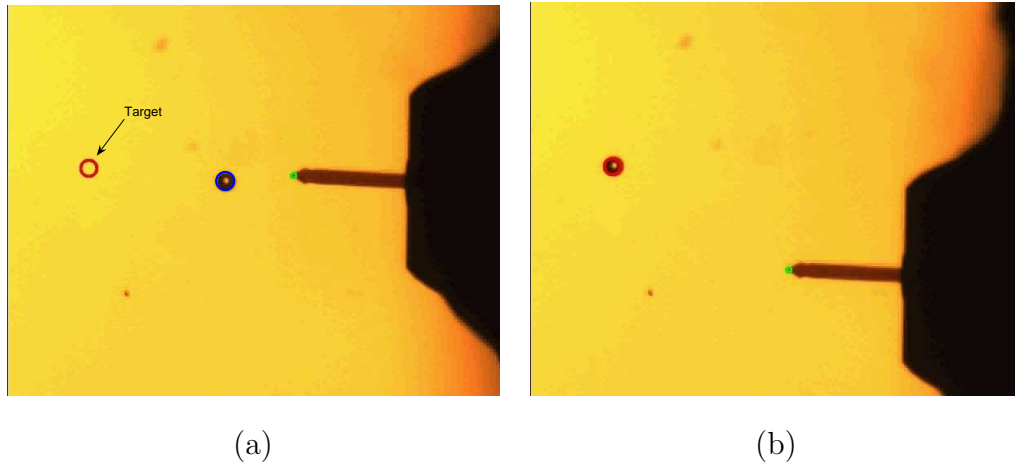


Figure 3.11: Automatic Micromanipulation of a Microsphere, (a) Initial Position, (b) Final Position

path and to generate different patterns.

3.3.1 Algorithm

The algorithm to achieve the desired pattern formation is given below:

1. The side camera determines the optimal z position by processing the sample stage scene and the probe is moved to the determined contact point in the x-z plane.
2. Workspace is explored, the particle and obstacle map are recorded before the workspace is occluded by the moving probe.
3. If there are not adequate microballs for predetermined pattern, the program is terminated.
4. The closest microsphere to the target is chosen as the first particle to be pushed so that there will be no obstacle along the pushing line.
5. Unless there is no obstacle along the line between the probe tip and center of the particle, the probe directly approaches to the destination at a given speed in the x-y plane. If any obstacle is detected, the obstacle avoidance determines the path until no obstacle exists along the way to the particle.
6. The probe is moved to the determined contact point in the x-y plane by having the visual feedback from the top camera.

7. The particle is pushed along the line which connects the center of the sphere to the target until the particle is located at the target.
8. After the recorded obstacle map (in the second step) is reprocessed, the probe is moved to its initial position directly, if there is no obstacle along the path to the initial position. If any obstacle is detected on the way, obstacle avoidance mode is activated until no obstacle exists along the line between the probe tip and its initial position.
9. Go to the Step 2 until the predetermined pattern is generated.

The serial micromanipulation process includes five stages such as z movement, explore, obstacle avoidance, pushing and home modes. In the z movement mode, the probe tip is positioned along the z axes by processing the workspace image acquired from the side camera. In the explore mode, probe is positioned such that all the workspace is visible and no occlusion occurs due to the probe position. Thus the global particle map can be extracted and used for the following steps. As the probe approaches to the determined particle, there may be an obstacle on the line to the destination. Then the region twice the size of the obstacle is surrounded by a rectangular path, and it is followed by the probe until no obstacle exists on the way to the particle. An illustrative figure is shown in Fig. 3.12.

In the home mode, the probe is moved to its initial position with the obstacle avoidance support so that the particle map in the workspace can be updated with no occlusion of the probe.

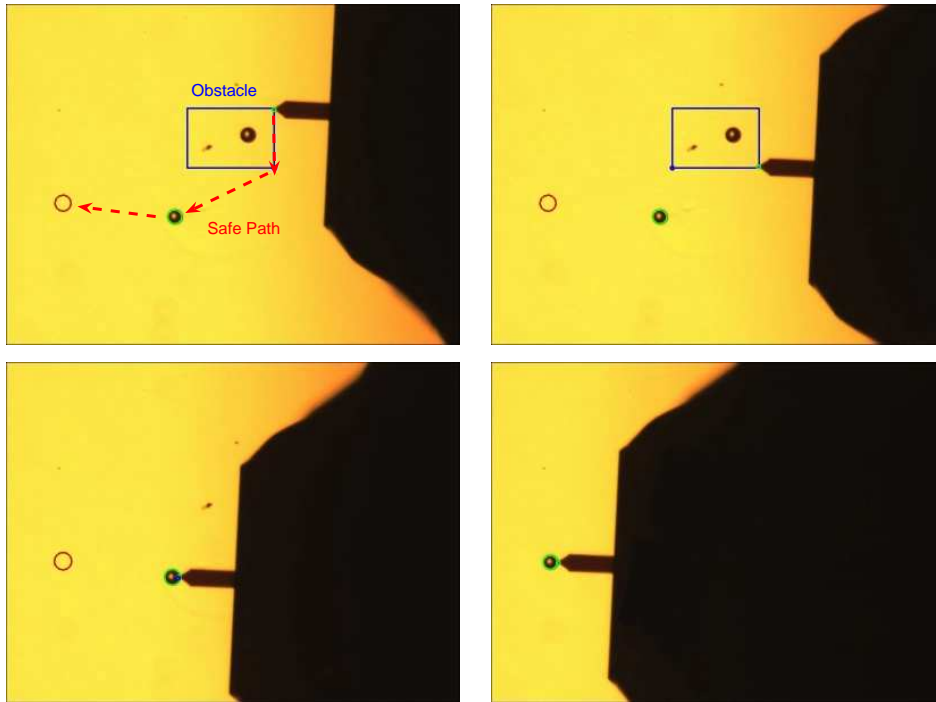


Figure 3.12: Obstacle Avoidance

Chapter 4

Parameter Estimation Schemes Using Vision and/or Force

4.1 Background

The problem of parameter estimation can be summarized as follows: Suppose that a set of candidate models have been selected, and this set is parameterized using a parameter vector θ . Searching for the best model within the set then turns into a θ estimation problem. In the literature, several methods were proposed to systemize such a search based on different priorities [39].

Having determined a model structure $M(\theta)$, the set of models using the parameter vector $\theta \in D_M \subset \mathfrak{R}^d$ is defined as,

$$M^* = M(\theta) \mid \theta \in D_M \quad (4.1)$$

Suppose that our system is described as

$$y(t) = G(q, \theta)u(t) + H(q, \theta)e(t) \quad (4.2)$$

where $y(t)$, q and $e(t)$ are the output of the system, the forward shift operator and a sequence of independent random variables with zero mean values and variances λ respectively. $G(q, \theta)$ is the transfer function of the system and $H(q, \theta)e(t)$ is the descriptor for additive disturbance.

Let a batch of data be collected from the system:

$$Z^N = [y(1), u(1), y(2), u(2), \dots, y(N), u(N)] \quad (4.3)$$

Now we are looking for a test to assess the ability of utilizing the information in the obtained data for different models. We can define a prediction error given by a certain model $M(\theta_*)$ to evaluate the prediction performance

$$\varepsilon(t, \theta_*) = y(t) - \hat{y}(t|\theta_*) \quad (4.4)$$

where $\hat{y}(t|\theta_*)$ is the predicted output for the model and these errors are computed for $t = 1, 2, \dots, N$. In order to understand the magnitude of the prediction error sequence, we can define a norm for the filtered $\varepsilon(t, \theta)$,

$$V_N(\theta, Z^N) = \frac{1}{N} \sum_{t=1}^N \ell(L(q)\varepsilon(t, \theta)) \quad (4.5)$$

where $\ell(\cdot)$ and $L(q)$ are a scalar-valued function and a linear stable filter respectively. Then the best estimate $\hat{\theta}_N$ can be computed as the minimization of (4.5),

$$\hat{\theta}_N = \arg \min_{\theta \in D_M} V_N(\theta, Z^N) \quad (4.6)$$

There are several methods to fit models in a given set to observed data which aim to minimize the prediction error sequence [39]:

- The prediction error identification approach (PEM) which was defined above contains well-known the least-squares (LS) method and the maximum likelihood (ML) method.
- The subspace approach to identifying state-space models consists of estimating the states from the given data and estimating the state-space matrices using the LS method.
- There is also an alternative approach called the correlation approach which contains the instrumental-variable (IV) technique.

In this chapter, some offline and online parameter estimation techniques are employed to identify optical parameters in the first two sections and to characterize the mechanical properties of the zebrafish embryos in the last section.

4.2 Optical System Calibration

In the Microassembly Workstation, the visual information is the crucial feedback type to enable the micro-manipulation and -assembly tasks. Processing the visual data determines the path of the end effector in the image frame, however the input of manipulator is given in its own frame. Thus the mapping between the manipulator frame and the image frame forms a critical component for servoing of the probe and

the gripper. In order to compute the mapping, a calibration method is developed and implemented.

Several calibration methods exist in the literature that are mostly used in macro scale vision applications [41], [42], [43]. However, these methods cannot directly be employed to calibrate an optical microscope coupled with a CCD camera due to the unique characteristics of the optical system. Large numerical apertures and high optical magnifications, and thus very small depth-of-field property of optical microscopes restricts the calibration to a single parallel plane. Because standard Tsai calibration requires the calibration pattern tilted at least 30 degrees and standard Zhang calibration needs at least three images of the model plane for different orientations, these methods could not propose a direct solution to the calibration of the optical microscope system [41], [42]. Modifications to Tsai's and Zhang's algorithms have resulted in several camera calibration algorithms ([44], [45], [46]) for optical microscope and camera systems.

The camera calibration for a near parallel case is proposed by Zhuang and Wu [44]. Under the assumption of small rotations of the camera about the axes (x and y), rotation angles (α and β) were linearized to simplify the extraction of the extrinsic parameters by the small angle approximation. However, this model cannot give accurate rotation angles and needs precalibration of the focal length which is not possible for the optical microscope system. The calibration of an optical microscope has been carried out by Zhou and Nelson that is based on the Tsai's model, specially modified for the parallel case and experimentally validated [45]. A further method is proposed by Ammi et al. that is based on Zhang's model and modified for a single image [46]. Instead of conventional calibration pattern, a virtual calibration pattern was constructed using a micromanipulator with sub-pixel localization in the image. However, these methods are computationally complex and cannot propose a solution for the close focus microscope, side view, since it does not have the same image forming components with a typical microscope. Thus, a generic calibration algorithm for the optical systems with high magnifications is designed based on weak perspective camera model and Tsai's algorithm [41].

In this method, the complex combination of the image forming elements in the optical pathway is modeled via a weak perspective camera model. Three coordinate

systems, objective (F^o), image (F^i) and world (F^w) coordinate systems, are used in this model, shown in Fig. 4.1. The origin of the objective coordinate system is the optical center point (o), the X^o and Y^o axes are aligned with the rows and columns of image frame respectively. The Z^o axis is aligned with the optical axis of the microscope. The origin of the image coordinate system is intersection of the virtual image plane with the optical axis and X^i , Y^i are parallel to the X^o and Y^o axes. The world frame can be chosen arbitrarily. However, it is more convenient to attach the frame to tip of the end effector.

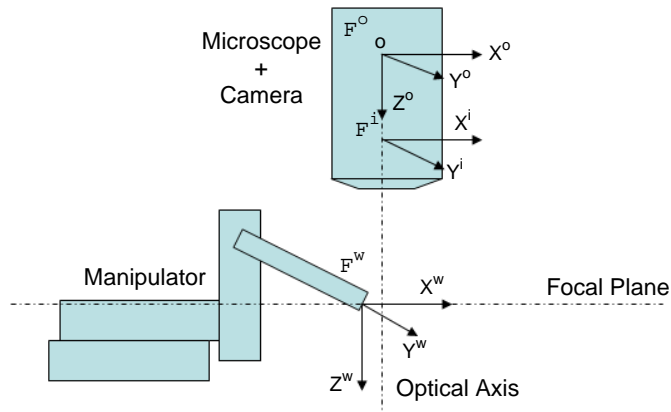


Figure 4.1: Assigned Image, Objective and World Coordinate Systems

The transformation from the world frame to the objective frame is given by a rotation matrix (R) and a translation vector (T)

$$\begin{pmatrix} X^o \\ Y^o \\ Z^o \end{pmatrix} = \begin{pmatrix} r_{11} & r_{12} & r_{13} \\ r_{21} & r_{22} & r_{23} \\ r_{31} & r_{32} & r_{33} \end{pmatrix} \begin{pmatrix} X_w \\ Y_w \\ Z_w \end{pmatrix} + \begin{pmatrix} T_x \\ T_y \\ T_z \end{pmatrix} \quad (4.7)$$

where

$$R = \begin{pmatrix} \cos \alpha \cos \beta & \cos \alpha \sin \beta \sin \gamma - \sin \alpha \cos \gamma & \cos \alpha \sin \beta \cos \gamma + \sin \alpha \sin \gamma \\ \sin \alpha \cos \beta & \sin \alpha \sin \beta \sin \gamma + \cos \alpha \cos \gamma & \sin \alpha \sin \beta \cos \gamma - \cos \alpha \sin \gamma \\ -\sin \beta & \cos \beta \sin \gamma & \cos \beta \cos \gamma \end{pmatrix}$$

and α, β, γ are the roll, pitch, yaw angles respectively.

We can write the image of a point (X^o, Y^o, Z^o) in the undistorted image coordinates (u', v') as

$$\begin{aligned} u' &= \frac{f}{s_x} \frac{X^o}{Z^o} + o_x \\ v' &= \frac{f}{s_y} \frac{Y^o}{Z^o} + o_y \end{aligned} \quad (4.8)$$

where f is the objective focal length, s_x and s_y are horizontal and vertical pixel sizes respectively, (o_x, o_y) are the coordinates of image center. Plugging the equation (4.7) into (4.8) gives

$$\begin{aligned} u' - o_x &= f_x \frac{r_{11}X^w + r_{12}Y^w + r_{13}Z^w + T_x}{r_{31}X^w + r_{32}Y^w + r_{33}Z^w + T_z} \\ v' - o_y &= f_y \frac{r_{21}X^w + r_{22}Y^w + r_{23}Z^w + T_y}{r_{31}X^w + r_{32}Y^w + r_{33}Z^w + T_z} \end{aligned} \quad (4.9)$$

where $f_x = f/s_x$ and $f_y = f/s_y$. Since the object plane is nearly parallel with the image plane and depth of the object itself is much smaller than the mean distance (\bar{Z}) along the optical axis, the undistorted image coordinates of an object can be written in the objective frame as

$$\begin{aligned} u' &\approx f_x \frac{X^o}{\bar{Z}} = M_x X^o \\ v' &\approx f_y \frac{Y^o}{\bar{Z}} = M_y Y^o \end{aligned} \quad (4.10)$$

where M_x and M_y are the magnifications along the x and y axes of the objective. It is assumed that only first term of radial distortion is dominant for the microscope. Thus

$$\begin{aligned} u' &= u(1 + \kappa_1 r^2) \\ v' &= v(1 + \kappa_1 r^2) \end{aligned} \quad (4.11)$$

where (u, v) are the distorted image coordinates of a point and κ_1 is the radial distortion coefficient. Combining the above equations gives the following relation between the image coordinates and world coordinates in terms of the parameters to be calibrated (assuming $Z^w = 0$)

$$\begin{aligned} u(1 + \kappa_1 r^2) &= M_x(r_{11}X^w + r_{12}Y^w + T_x) \\ v(1 + \kappa_1 r^2) &= M_y(r_{21}X^w + r_{22}Y^w + T_y) \end{aligned} \quad (4.12)$$

Now we can start to solve for the unknown parameters. The first step of the algorithm employs the Radial Alignment Constraint (RAC) from Tsai's algorithm [41]. For each point i with (X^{wi}, Y^{wi}, Z^{wi}) and (u_i, v_i) as the 3D world coordinate and the corresponding image coordinate, we can write the following relation using 4.12

$$\begin{pmatrix} v_i X_{wi} & v_i Y_{wi} & v_i & -u_i X_{wi} & -u_i Y_{wi} \end{pmatrix} \begin{pmatrix} T_y^{-1} r_{11} \\ T_y^{-1} r_{12} \\ T_y^{-1} T_x \\ T_y^{-1} r_{21} \\ T_y^{-1} r_{22} \end{pmatrix} = u_i \quad (4.13)$$

Using five or more points, we can solve for $T_y^{-1}r_{11}, T_y^{-1}r_{12}, T_y^{-1}T_x, T_y^{-1}r_{21}, T_y^{-1}r_{22}$. Considering that the rotation matrix (R) is orthonormal with determinant $+1$, T_y can be computed as

$$T_y^2 = \frac{S_r - [S_r^2 - 4(r'_{11}r'_{22} - r'_{21}r'_{12})^2]^{\frac{1}{2}}}{2(r'_{11}r'_{22} - r'_{21}r'_{12})^2} \quad (4.14)$$

where r'_{ij} is scaled r_{ij} and $S_r = r'_{11}{}^2 + r'_{12}{}^2 + r'_{21}{}^2 + r'_{22}{}^2$. After the scale factor is obtained, (T_x, T_y) can be computed and the rotation matrix can be recovered with the following formula

$$R = \begin{pmatrix} r_{11} & r_{12} & (1 - r_{11}^2 - r_{12}^2)^{\frac{1}{2}} \\ r_{21} & r_{22} & s(1 - r_{21}^2 - r_{22}^2)^{\frac{1}{2}} \\ r_{31} & r_{32} & r_{33} \end{pmatrix} \quad (4.15)$$

where $s = -sgn(r_{11}r_{21} + r_{12}r_{22})$ and third row can be computed as cross product of the first two rows. It is straightforward to recover T_x .

In the second step, the total magnification (M) of the system and the radial distortion coefficient (κ_1) can be obtained by a least square solution. Note that the aspect ratio ($a = s_y/s_x$) is assumed to be unity without loss of generality. Let

$$\begin{aligned} m &= r_{11}X^w + r_{12}Y^w + T_x \\ n &= r_{21}X^w + r_{22}Y^w + T_y \end{aligned} \quad (4.16)$$

Combining (4.12) and (4.16) gives a homogenous linear system,

$$M(m + n) - \kappa_1(u + v)r^2 - (u + v) = 0 \quad (4.17)$$

Rewriting the Eq.(4.17) gives

$$\begin{pmatrix} m + n & -(u + v)r^2 \end{pmatrix} \begin{pmatrix} w_1 \\ w_2 \end{pmatrix} = u + v \quad (4.18)$$

where $w_1 = \hat{\kappa}_1$ and $w_2 = \hat{M}$ can be solved by a least square method.

4.2.1 Selection of Calibration Pattern

Camera calibration methods use reference calibration patterns with known geometry. The correspondence between the geometry of the pattern and the extracted features from the image of this pattern are used to compute the camera calibration

parameters. The precision of the calibration pattern design plays an important role in the accuracy of calibration. In addition to designing precise 3D points, using robustly extractable image features is also important to establish the correspondence. Moreover, employing more correspondences in calibration improves the quality of calibration.

In the literature, several calibration patterns with a variety of geometry (2D/3D), shapes (circular/square) and geometric primitives (point/line) are reported. However, number of calibration pattern designs are limited in microscopy literature due to the small depth of field of light microscopes. Zhou et al. [45] uses microfabricated square arrays in various sizes. For every magnification level, they assign different square sizes. This pattern contains a large number of calibration points which are extracted using robust image processing algorithms. Ammi et al. [46] use the tip of the micromanipulator to construct a virtual calibration pattern. The 3D position of the AFM tip is determined from the position of micromanipulator with 100 nm nominal positioning precision.

In this setup, two lithographically etched glass calibration patterns with square and circle grids and a virtual calibration pattern are employed to calibrate the optical system. These patterns are shown in Fig.4.2 . The square and circular ones have many robustly extractable image features. For the square one, a Sobel edge operator, edge linking and then a line fitting algorithm were applied to obtain every edge line of the squares. Corners of the squares -intersections of the calculated edge lines- were taken as the calibration points. For the round calibration grid, the center coordinates of the circles were calculated through a least square solution. Using static calibration patterns are not practical in microsystems due to the difficulty of installing and removing the pattern in a small workspace. Moreover, each magnification level requires patterns in different sizes. Another drawback is that the static patterns cannot be employed to calibrate the lateral microscope. Constructing a virtual calibration pattern with moving the manipulator is another alternative. Although the lithographically etched glass calibration patterns are manufactured in the precision of ∓ 2 microns, the micromanipulator can provide 50 nm nominal positioning precision. Thus, the tip detection algorithm probably determines the precision of the correspondence. In addition to intrinsic parameters, using manip-

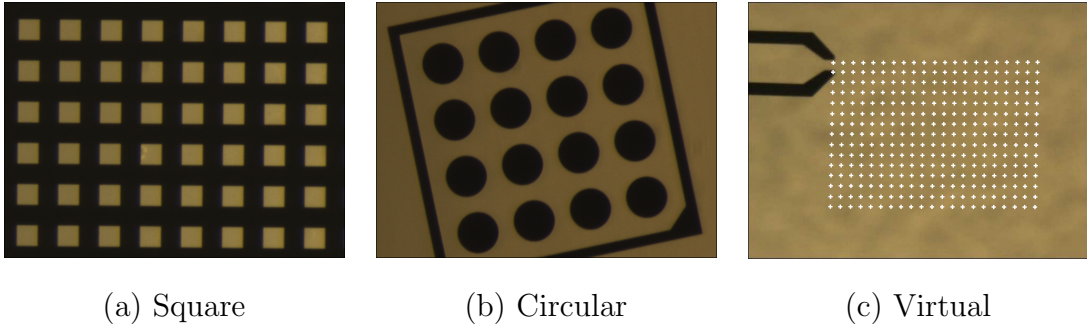


Figure 4.2: Calibration Patterns

ulator data provides the rotation and translation between the manipulator and the objective frame which is crucial for the visual servoing applications. Furthermore, it is possible to calibrate the system under every magnifications for the top and lateral microscopes. Therefore, moving the micromanipulator to establish a calibration pattern has many advantages over the static ones in microscope calibration.

4.2.2 Novel Calibration Algorithm

The algorithm which calibrates the optical system using a virtual pattern is given as follows:

1. The end effector is detected using a template matching method and is started to be tracked.
2. The controller generates a number of points for the end effector which corresponds to the corners of a virtual calibration grid.
3. For each given position, the image coordinates of the probe/gripper is computed using the Normalized Cross Correlation (NCC) technique.
4. Once the positions of the end effector in camera and manipulator space are collected, the Radial Alignment Constraint (RAC) [41] is employed to compute the rotation and translation from the manipulator coordinate frame to the image coordinate frame.
5. The total magnification (M) of the system and the radial distortion coefficient (κ_1) can be obtained by a least square solution which minimizes the equation (4.17).

4.3 Online Optical System Calibration

In vision based micromanipulation and assembly applications, transporting mesoscale objects within micron or submicron accuracies and assembling parts at different sizes may require coarse to fine manipulation strategies. During these tasks, the objects may need to be monitored and tracked under different optical magnifications. Thus the optical microscope must be calibrated for each zoom level to effectively use visual feedback in micromanipulation and assembly tasks. A look-up table for different optical settings can be generated to relate world and image coordinates. However, constructing a look-up table is time consuming, and a very small change in position or orientation of optical or mechanical components in the workcell requires the reconstruction of the look-up table. Therefore an online optical calibration scheme is proposed to overcome the drawbacks of generating a look-up table in this section. Since none of the optical microscope calibration methods ([45], [46]) in the literature can be used for an online calibration procedure, a new formulation of optical microscope calibration via a recursive least square method is presented.

4.3.1 Estimation of Projection Matrix

The geometrical relation between the 3D coordinates (X^w, Y^w, Z^w) of a point in space and 2D coordinates (u, v) of its projection on the image plane can be written by employing a 3×4 projection matrix P ,

$$\begin{pmatrix} x_i \\ y_i \\ w_i \end{pmatrix} = P \begin{pmatrix} X_i^w \\ Y_i^w \\ Z_i^w \end{pmatrix} \quad (4.19)$$

with

$$\begin{aligned} u_i &= \frac{x_i}{w_i} = \frac{p_{11}X_i^w + p_{12}Y_i^w + p_{13}Z_i^w + p_{14}}{p_{31}X_i^w + p_{32}Y_i^w + p_{33}Z_i^w + p_{34}} \\ v_i &= \frac{y_i}{w_i} = \frac{p_{21}X_i^w + p_{22}Y_i^w + p_{23}Z_i^w + p_{24}}{p_{31}X_i^w + p_{32}Y_i^w + p_{33}Z_i^w + p_{34}} \end{aligned} \quad (4.20)$$

Note that i denotes the i^{th} point in space and its projection in pixels.

Since the optical and mechanical components of micromanipulation workstations are designed and machined very precisely, it is assumed that top surface of the sample stage is perpendicular to the optical axis of the CCD camera. Moreover, the depth

of an object which is placed under a microscope is usually much smaller than the mean distance (\bar{Z}) along the optical axis. Thus (4.20) is rewritten as

$$\begin{aligned} u_i &\approx \frac{p_{11}X_i^w + p_{12}Y_i^w + p_{14}}{\bar{Z}} \\ v_i &\approx \frac{p_{21}X_i^w + p_{22}Y_i^w + p_{24}}{\bar{Z}} \end{aligned} \quad (4.21)$$

Note that $Z^w = 0$ is assumed. Transforming (4.21) into a linear system gives

$$\begin{pmatrix} u_i \\ v_i \end{pmatrix} = P \begin{pmatrix} X^w \\ Y^w \\ 1 \end{pmatrix} \quad (4.22)$$

where $P \in \mathfrak{R}^{2 \times 3}$.

Eq. (4.22) can be recasted linearly in terms of the entries of P matrix as follows:

$$y = \varphi^T \theta \quad (4.23)$$

$$\text{where } y = \begin{pmatrix} u_i \\ v_i \end{pmatrix}, \varphi = \begin{pmatrix} X_i^w & Y_i^w & 1 & 0 & 0 & 0 \\ 0 & 0 & 0 & X_i^w & Y_i^w & 1 \end{pmatrix}^T \text{ and}$$

$$\theta = \begin{pmatrix} p_{11} & p_{12} & p_{13} & p_{21} & p_{22} & p_{23} \end{pmatrix}^T$$

In order to solve for the parameter vector θ , φ matrix has to be nonsingular. Thus, one can assign at least three points with known world and image coordinates to provide a nonsingular φ matrix. However, computing the coordinates of multiple points in a single frame with only one encoder output requires a precise CAD and the orientation of the end effector which is being tracked during the calibration. On the other hand, assuming the transformation parameters are constant for three consecutive frames, the regressor matrix φ can become a square matrix. Augmenting φ matrix with two previous measurements gives

$$\underbrace{\begin{pmatrix} u_k \\ v_k \\ u_{k-1} \\ v_{k-1} \\ u_{k-2} \\ v_{k-2} \end{pmatrix}}_y = \underbrace{\begin{pmatrix} X_k^w & Y_k^w & 1 & 0 & 0 & 0 \\ 0 & 0 & 0 & X_k^w & Y_k^w & 1 \\ X_{k-1}^w & Y_{k-1}^w & 1 & 0 & 0 & 0 \\ 0 & 0 & 0 & X_{k-1}^w & Y_{k-1}^w & 1 \\ X_{k-2}^w & Y_{k-2}^w & 1 & 0 & 0 & 0 \\ 0 & 0 & 0 & X_{k-2}^w & Y_{k-2}^w & 1 \end{pmatrix}}_{\varphi^T} \underbrace{\begin{pmatrix} p_{11} \\ p_{12} \\ p_{13} \\ p_{21} \\ p_{22} \\ p_{23} \end{pmatrix}}_{\theta} \quad (4.24)$$

where the redefined $y \in \mathfrak{R}^6$ and $\varphi \in \mathfrak{R}^{6 \times 6}$.

Suppose that the observed data actually have been generated by (4.24), we can define our predictor as,

$$\hat{y}(t|\theta) = \varphi(t)^T \hat{\theta}(t) \quad (4.25)$$

With (4.25) the prediction error becomes

$$\varepsilon(t, \theta) = \varphi(t)^T \theta(t) - \varphi(t)^T \hat{\theta}(t) \quad (4.26)$$

and the criterion function resulting from (4.5) with $L(q) = 1$ is

$$V_N(\theta, Z_N) = \frac{1}{N} \sum_{t=1}^N \ell(\theta, t) \quad (4.27)$$

Since there is no guarantee that the added points to φ carry sufficient information in practice, the problem of minimizing V_N may be ill-conditioned in the sense that φ matrix may not be full rank. Thus, V_N can be modified by adding a cost on the squared distance between θ and θ^0 which is a fixed point in the parameter space.

$$W_N(\theta, Z_N) = V_N + \delta \|\theta - \theta^0\|^2 = \frac{1}{N} \sum_{t=1}^N \ell(\varepsilon(\theta, t)) + \delta \|\theta - \theta^0\|^2 \quad (4.28)$$

Moreover, it may happen that measurements at different time instants are considered to be of varying reliability. The reason may be that the degree of noise corruption changes or that certain measurements are less representative for the system's properties. In such cases, the norm ℓ be time varying:

$$W_N(\theta, Z_N) = \frac{1}{N} \sum_{t=1}^N \ell(\varepsilon(\theta, t), \theta, t) + \delta \|\theta - \theta^0\|^2 \quad (4.29)$$

Using a weighting function $\beta(N, t)$, the different measurements could be assigned different weights. The new W_N can be redefined with $\ell(\varepsilon) = \frac{1}{2}\beta(N, t)\varepsilon^2$ as

$$W_N(\theta, Z_N) = \frac{1}{N} \sum_{t=1}^N \frac{1}{2} \beta(N, t) ([y(t) - \varphi^T(t)\theta]^2 + \delta \|\theta - \theta^0\|^2) \quad (4.30)$$

The estimate that minimizes the criterion in (4.30) is

$$\check{\theta}_t = \arg \min \sum_{t=1}^N \frac{1}{2} \beta(N, t) ([y(t) - \varphi^T(t)\theta]^2 + \delta \|\theta - \theta^0\|^2) \quad (4.31)$$

This is given by

$$\check{\theta}_t = \bar{R}^{-1}(t) f(t) \quad (4.32)$$

$$\bar{R}(t) = \sum_{k=1}^t \beta(t, k) [\varphi(k)\varphi^T(k) + \delta I] \quad (4.33)$$

$$f(t) = \sum_{k=1}^t \beta(t, k) [\varphi(k)y(k) + \delta\theta^0] \quad (4.34)$$

It is also important to have the parameters of the system available online, while the system is in operation. Let the weighting sequence has the following property

$$\begin{aligned} \beta(t, k) &= \lambda(t)\beta(t-1, k) \quad 0 \leq k \leq t-1 \\ \beta(t, t) &= 1 \end{aligned} \quad (4.35)$$

(4.32)-(4.34) are rewritten as a recursive algorithm

$$\hat{\theta}_t = \hat{\theta}_{t-1} + \bar{R}^{-1}(t) f(t) \quad (4.36)$$

$$\bar{R}(t) = \lambda(t)\bar{R}(t-1) + \varphi(t)\varphi^T(t) + \delta I \quad (4.37)$$

$$f(t) = \lambda(t)f(t-1) + \varphi(t)y(t) + \delta\theta^0 \quad (4.38)$$

4.3.2 Computing Optical System Parameters

Having recovered the projection matrix P from the estimate θ , the entries of the projection matrix can now be related to the intrinsic and extrinsic optical system parameters by using (4.9) and (4.10),

$$P = \begin{pmatrix} M_x r_{11} & M_x r_{12} & M_x T_x \\ M_y r_{21} & M_y r_{22} & M_y T_y \end{pmatrix} \quad (4.39)$$

Since the image center (o_x, o_y) is assumed to be known, it is not explicitly shown in (4.39). Assuming that the aspect ratio $(\alpha = s_y/s_x)$ is unity, $r_{11}, r_{12}, r_{21}, r_{22}$ can be obtained up to a scale. Using the equations (4.13)-(4.15), magnification, the three rotation angles, T_x, T_y can be computed.

4.4 Force Estimation

4.4.1 Background

In dexterous micromanipulation tasks, the ability of monitoring, positioning and transforming the object is usually required. Although, some successful experiments with only monitoring and positioning objects were reported in [5], [10], [24], [25], more complex manipulation scenarios demand an additional force information to provide high dexterity. Force sensing is specifically important for biomanipulation tasks, since the cells and tissues involved are often fragile and easily damaged. Thus pure positioning control cannot usually guarantee a successful operation without damaging the object in a biomanipulation task. On the other hand, some applications in particular aim to obtain force information to understand the forces between the manipulator and object. In these applications, quantitative force measurements are employed to understand the material property information and to characterize the objects. Especially, measuring force on a cell and/or tissue membrane are important for understanding relationship between mechanical forces and structural deformations which hold potential for studies on zona hardening, polyspermy and implantation failures in mammals.

Force measurement in microscale is usually done by measuring the change in certain properties of the sensing element such as strain gauge, piezoelectric, capacitive sensors or using laser-based optical techniques such as atomic force microscope [20]. Furthermore, some works [21] and [47] propose vision-based force measurement as an alternative method which has the advantage of using the already existing microscope optics and cameras in a micromanipulation workstation. In [21], Kaneko et al. reports an intraocular pressure estimation method by using the obtained cornea deformation from image and the nonlinear cornea model. In [47], the author presents a method to visually measure the force distribution applied to a linearly elastic object using the contour data in an image. On the other hand, some works employ both a force sensor and vision algorithms to understand the mechanical properties of microobjects. In [11], a two-axis cellular force sensor and structural deformations on both mouse oocytes and embryos obtained from a microscope are used describe the mechanical properties of the mouse zona pellucida based on a biomembrane me-

chanical model. Same biomembrane model is utilized to understand the evolution of the chorion for the different developmental stages of zebrafish in [13]. The point load biomembrane model in [11] and [13] assumes that the cell starts with a planar circular area with zero residual stress and deformed in a symmetric way along the micropipette, however, all the cellular structures are not symmetrical. Moreover, the dynamical effects are not considered during a micromanipulation task in this model.

4.4.2 Estimation Model

We propose a new approach to estimate the mechanical properties of cellular structures which uses vision and force information. In this method, not only the static but also dynamic effects are considered using a nonlinear mass-spring-damper model. Thus, the computed parameters can be utilized to estimate the imposed force on a biomembrane and provide the adequate information to control the position, velocity and acceleration of the probe without damaging the cell or tissue during a micromanipulation task.

The one dimensional mass-spring-damper model with a hardening spring, illustrated in Fig. 4.3 is given as,

$$F = m\ddot{x} + b\dot{x} + k_1x + k_2x^3 \quad (4.40)$$

where F is the applied force, m , b , k_1 and k_2 are the mass, damping, first and second spring coefficients of the object which is being manipulated.

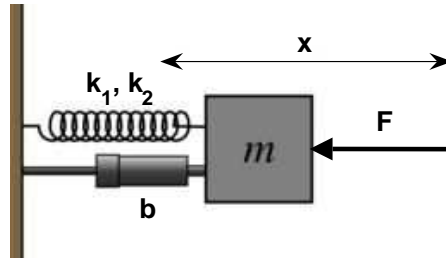


Figure 4.3: Nonlinear Mass-Spring-Damper Model

Assuming that the applied force, acceleration, velocity and position of the object are known, (4.40) can be rewritten linearly in terms of the unknown m , b , k_1 and k_2 parameters as follows,

$$F = \underbrace{\begin{pmatrix} \ddot{x} & \dot{x} & x & x^3 \end{pmatrix}}_{\varphi^T} \underbrace{\begin{pmatrix} m \\ b \\ k_1 \\ k_2 \end{pmatrix}}_{\theta} \quad (4.41)$$

Since measuring the force for multiple points in each iteration with a single force sensor output is not possible, assuming that the unknown parameters are constant for at least four time steps, φ can be expanded to a square or overdetermined matrix by concatenating force and deformation measurements from these time steps,

$$\begin{pmatrix} F_n \\ F_{n-1} \\ F_{n-2} \\ F_{n-3} \end{pmatrix} = \underbrace{\begin{pmatrix} \varphi_n^T \\ \varphi_{n-1}^T \\ \varphi_{n-2}^T \\ \varphi_{n-3}^T \end{pmatrix}}_{\varphi^T} \underbrace{\begin{pmatrix} m \\ b \\ k_1 \\ k_2 \end{pmatrix}}_{\theta} \quad (4.42)$$

where n is the n^{th} time step, $\varphi_i = \begin{pmatrix} \ddot{x}_i & \dot{x}_i & x_i & x_i^3 \end{pmatrix}^T$ and the redefined $\varphi \in \mathfrak{R}^{4 \times 4}$.

Although θ vector can be solved with the standard least squares, φ may be ill-conditioned or yielding many solutions. In order to compute θ with desirable properties, the cost function is given with a regularization term,

$$\varepsilon = \| F - \varphi^T \theta \|^2 + \delta \| \theta - \theta^0 \|^2 \quad (4.43)$$

where δ is a positive scalar. Adding the regularization term $\delta \| \theta - \theta^0 \|^2$ to the linear regression improves the robustness of the algorithm. Since the force and the spatial measurements are often distorted by noise, the regularization may enhance the condition number of φ matrix. Assuming θ^0 is the origin, an explicit solution, denoted by $\check{\theta}$, is given as,

$$\check{\theta} = (\varphi \varphi^T + \delta I)^{-1} \varphi F \quad (4.44)$$

where $I \in \mathfrak{R}^{4 \times 4}$ is the identity matrix.

Chapter 5

Experimental Results and Discussion

In this chapter, the experimental results of the previously explained micromanipulation and parameter estimation methods are presented. In the first part, the micromanipulation experiments which employ vision and force feedback are demonstrated. In the second part, offline and online optical system calibration, and force estimation results are given and discussed.

5.1 Micromanipulation Using Vision and Force

Before the microobject manipulation experiments are shown, the experimental results using only vision feedback without touching any microobjects are shown to validate that visual servoing ensures the required accuracy and precision for the manipulation tasks.

5.1.1 Visual Servoing Experiments

In order to evaluate the performances of the presented visual servoing algorithm with the optimal control synthesis which penalizes the error and the control signal, regulation and path following experimental results are given. In the experiments, the center of the microgripper opening is tracked with subpixel accuracy at 30 Hz. Micropositioning and trajectory following tasks are performed at 1X and 4X zoom levels. An illustrative figure is depicted in Fig. 5.1. For the optimal control design, Q and L matrices in (3.7) were chosen as diagonal matrices with diagonal entries (0.9,0.9) and (0.025, 0.05) respectively. Micropositioning visual servoing results are plotted in Figs. 5.2-5.3, and the trajectory following results for circular, square and sinusoidal trajectories are depicted in Figs. 5.4-5.6.

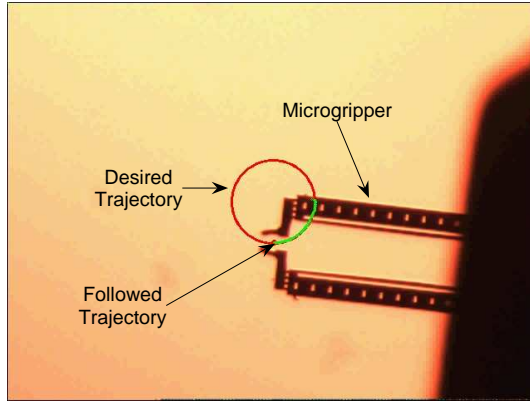


Figure 5.1: Circular Path Following Task at 1X

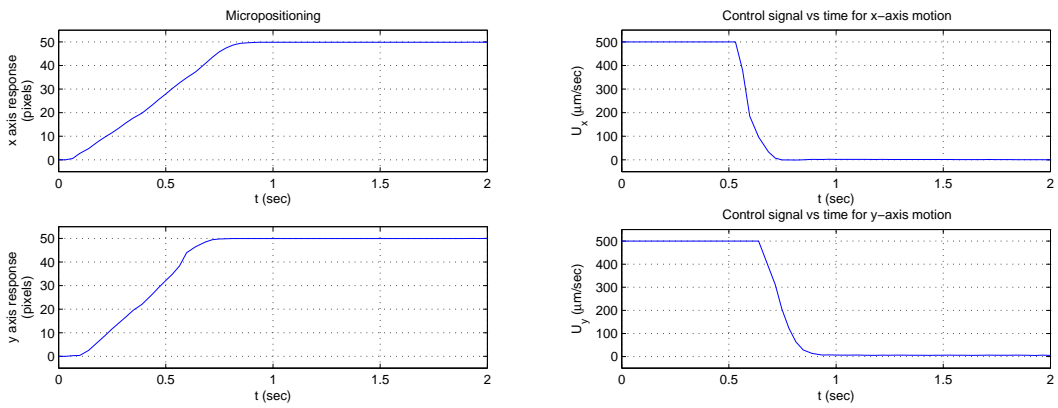


Figure 5.2: Step responses and control signals at 1X

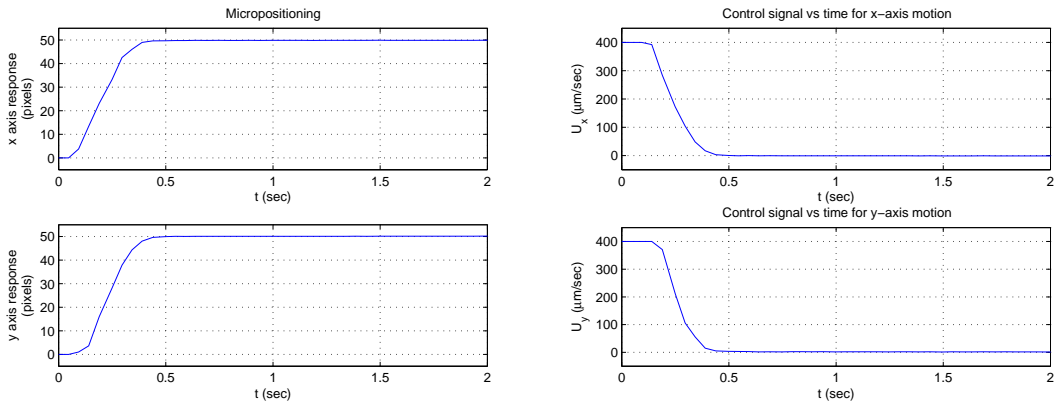


Figure 5.3: Step responses and control signals at 4X

For the micropositioning task, regulation performances at 1X and 4X for a step input of 50 pixels along the x and y axis of the objective frame in terms of settling time (t_s), accuracy and precision are tabulated in Table 5.1. For the trajectory following task, tracking performances for different trajectories (square, circular and

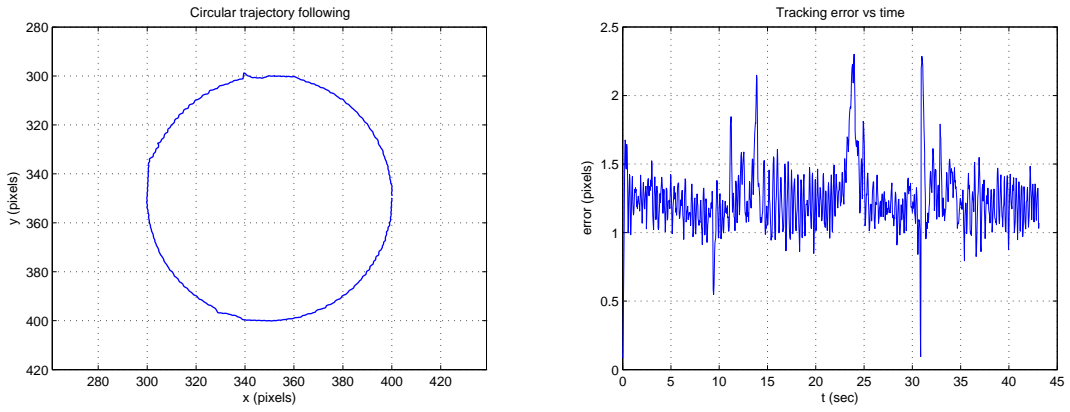


Figure 5.4: Circular trajectory and tracking error at 1X

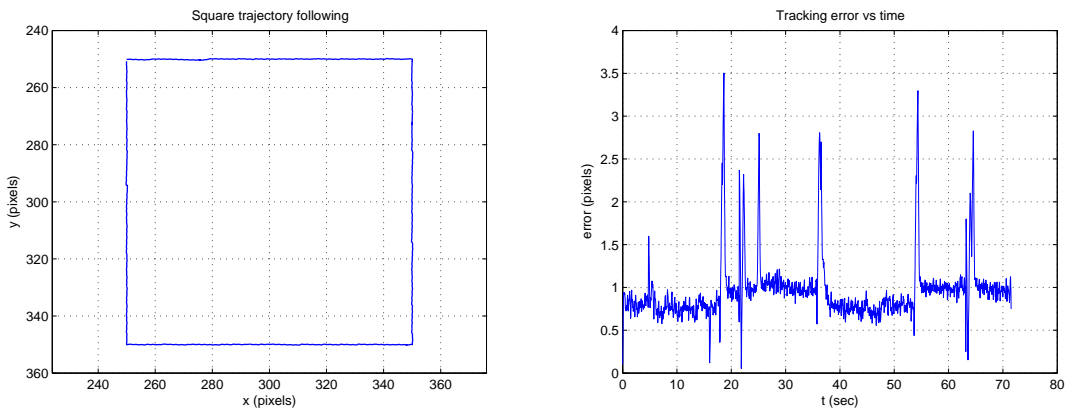


Figure 5.5: Square trajectory and tracking error at 1X

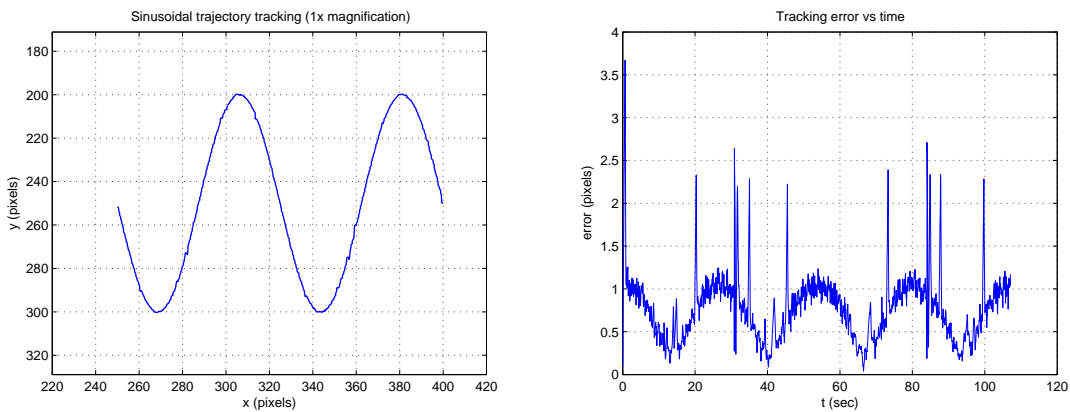


Figure 5.6: Square trajectory and tracking error at 1X

sinusoidal) are presented in Table 5.2.

The presented visual servoing guarantees convergence to the desired targets with

Table 5.1: Micropositioning Accuracy and Precision

	Step (pixels)	t_s (<i>sec</i>)	Acc. (μm)	Prec. (μm)
1 <i>x</i>	50	0.80	9.86	2.71
4 <i>x</i>	50	0.45	1.35	0.57

Table 5.2: Trajectory Tracking Accuracy and Precision

	Square		Circular		Sinusoidal	
	Acc. (μm)	Prec. (μm)	Acc. (μm)	Prec. (μm)	Acc. (μm)	Prec. (μm)
1 <i>x</i>	5.93	2.28	7.72	1.40	4.79	2.37
4 <i>x</i>	1.47	1.19	1.57	0.95	1.12	1.31

sub-micron error and satisfactory settling time. Moreover, the tracking performance also meets the requirements for a typical micromanipulation task which tolerates a few micron errors. Thus, it is shown that the presented method is proved to be practical for the assigned micromanipulation tasks in the following sections.

5.1.2 Micromanipulation Experiments

In order to validate the proposed the collision-free micromanipulation method, polystyrene balls are pushed on the sample stage to the desired locations. Before the experiments, the polystyrene balls on the glass surface are scattered by evaporating the water in the prepared diluted polystyrene-water solution. Distilled water is preferred in the solution to prevent the contamination of unwanted substances on the substrate surface. In the experiments, a tipless AFM probe is chosen to push the individual microballs. After the user determines the target locations, automatic micromanipulation algorithm starts. In the following experiment, the operator chooses a pattern in which the centers of three microspheres are on a same straight line.

In the first step, the probe moves to the computed position in the z direction to push the microsphere from a convenient contact point, shown in Fig. 5.7. In the

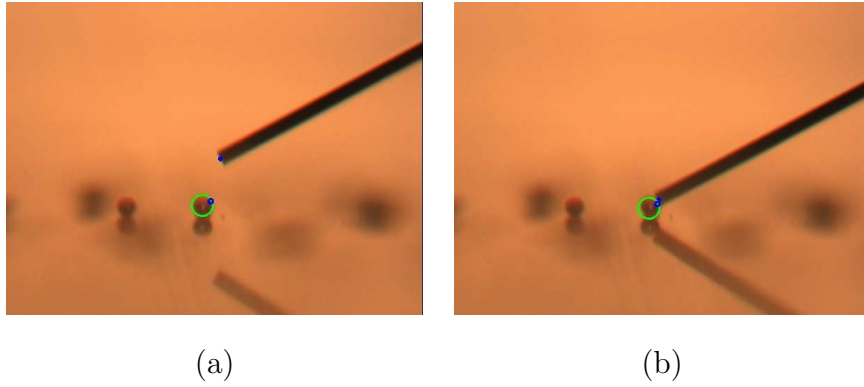


Figure 5.7: Visual Servoing in the x-z Plane

following steps, the microballs are pushed to the targets in the generated pattern using the explained motion planning method in Section 3.3.1. A summary of the experiment that illustrates the steps of the automatic micromanipulation task is given in Fig. 5.8.

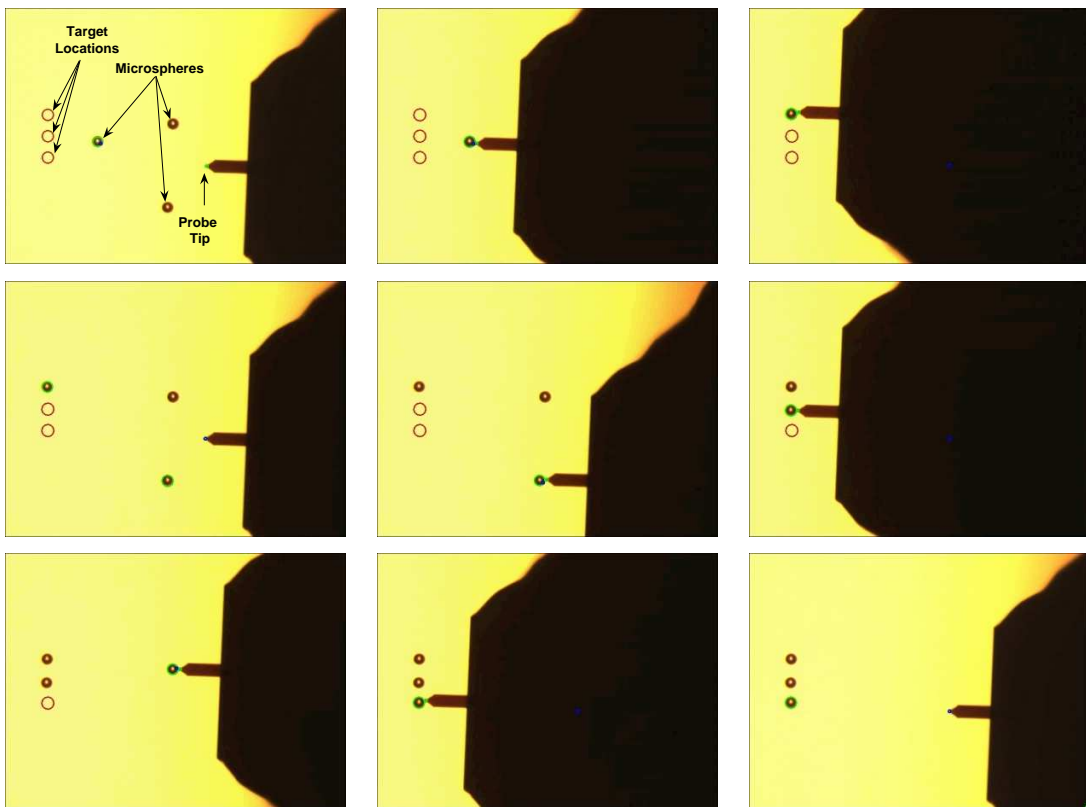


Figure 5.8: Automatic Micromanipulation of Microspheres

In the experiments, the 70 micron diameter microspheres can be transported to the desired locations with the accuracy of one pixel which is the tolerance defined by the user. The accuracy of the pushing experiments can be improved to 0.7 micron,

which is the resolution of the optical microscope, using the presented subpixel detection algorithms. Therefore a micromanipulation experiment in the microassembly workstation with the designed mechanical and software components is successfully demonstrated.

5.2 Parameter Estimation

5.2.1 Optical System Calibration Results

The presented calibration algorithm is implemented to calibrate the top view at 0.75X and 3X zoom levels and the side view. Three types of calibration patterns - square, circular and virtual - are employed to establish the correspondence between the world and image coordinates. These correspondences are used to obtain the extrinsic and intrinsic parameters of the optical system. While the intrinsic parameters which are computed using each pattern are useful, the extrinsic parameters which are obtained only from the virtual pattern can be used in the micromanipulation tasks. Because the visual servoing experiments require the rotation and translation between the optical system and the end effectors. Thus, the configurations of the static calibration patterns are not needed for any practical use. The calibration results for the square and circular patterns, and virtual patterns at 0.75X and 3X are given in Tables 5.3 and 5.4 respectively.

	Square		Circular	
	0.75X	3X	0.75X	3X
M	0.8995	3.5904	0.9017	3.5833
κ_1 (μm^{-2})	9.5181e-11	1.5e-11	4.2764e-9	-1.3278e-10
α (deg)	90.3695	90.5829	2.4364	-0.0304
β (deg)	-0.9639	-0.9203	2.9000	1.3852
γ (deg)	-176.3423	176.7221	4.2983	-2.5779
T_x (μm)	-1531.2	-378.1069	-546.4123	-289.0384
T_y (μm)	-1145.9	-269.3238	198.6936	-115.7292

Table 5.3: Computed Calibration Parameters using Square and Circular Patterns for Top View

	Gripper		Probe		Sample Stage	
	0.75X	3X	0.75X	3X	0.75X	3X
M	0.9071	3.6183	0.9219	3.6190	0.8982	3.5955
κ_1 (μm^{-2})	-3.7467e-9	-2.4550e-10	-3.2170e-11	-8.5130e-10	-9.4570e-11	1.9233e-9
α (deg)	0.0587	-1.9556	-0.7232	-0.6913	-0.3484	-0.7259
β (deg)	10.0806	7.9851	12.8347	5.2715	1.6289	1.7085
γ (deg)	-5.8712	-14.0889	2.0572	4.4215	-6.6549	-8.0929
T_x (μm)	-825.3126	-503.7519	-1362.6	-1333.9	-1362.6	-552.6890
T_y (μm)	-656.1795	-841.4709	-746.5861	-813.5869	-1041.1	-240.8963

Table 5.4: Computed Calibration Parameters using Virtual Patterns for Top View

The results of the generated virtual patterns by the gripper and probe for the side view calibration is also depicted in Table 5.5.

	Gripper	Probe
M	1.9012	1.9053
κ_1 (μm^{-2})	-3.2655e-9	5.1398e-010
α (deg)	0.1013	0.9528
β (deg)	-11.9959	-12.9723
γ (deg)	-88.1820	-90.9111
T_x (μm)	-705.2433	-536.5940
T_y (μm)	-590.1471	-427.9290

Table 5.5: Computed Calibration Parameters using Virtual Patterns for Side View

To judge the performance of the presented calibration algorithm using the given results, an error function is defined as

$$\epsilon = \frac{\sum^N [(u_i - \tilde{u}_i)^2 + (v_i - \tilde{v}_i)^2]^{1/2}}{N} \quad (5.1)$$

where N are the total number of points, (u_i, v_i) are image coordinates of i^{th} point and $(\tilde{u}_i, \tilde{v}_i)$ are the reprojected world coordinates for the computed rotation and translation in pixels. The error can also be converted to metric values by using the cell sizes and the computed magnification.

The computed reprojection errors for the static and virtual patterns are depicted in Tables 5.6 and 5.2.1 respectively. In the experiments the circle grids give more

	Square		Circular	
	0.75X	3X	0.75X	3X
Mean Error (μm)	1.0471	0.2920	0.8644	0.0552
Std Error (μm)	0.5099	0.1473	0.5106	0.0285
Maximum Error (μm)	3.5460	0.6586	1.7038	0.0992

Table 5.6: Reprojection Errors of Circular and Square Patterns for Top View

accurate calibration results than the circular ones. The result can be explained with the fact that the image might be blurred by a point spread function (PSF) and the features might not be extracted very accurately due to imperfect illumination, lens aberration, systematic and random sensor errors. Flusser et al. [48] claim that most of the PSF are circularly symmetric and circular shapes are invariant to this type of PSF. In Table 5.2.1, the reprojection errors for the generated virtual patterns for

	Gripper		Probe		Sample Stage	
	0.75X	3X	0.75X	3X	0.75X	3X
Mean Error (μm)	2.5823	1.4185	1.5506	0.6735	1.4185	0.7344
Std Error (μm)	0.9937	0.7395	0.5424	0.3745	0.7395	0.3923
Max Error (μm)	4.6908	3.1540	2.9244	1.8468	3.1540	1.7438

Table 5.7: Reprojection Errors of Virtual Patterns for Top View

the side view are given.

	Gripper	Probe
Mean Error (μm)	1.6998	0.7931
Std Error (μm)	0.8955	0.3078
Max Error (μm)	4.2666	1.4640

Table 5.8: Reprojection Errors of Virtual Patterns for Side View

It is observed that the static patterns give more accurate results due to the

fact that the image features for the static ones can be computed in a more robust manner. Since the end effectors are inclined to reach the workspace effectively, the detection algorithms may lead to inaccurate results when the probe is approaching to the limits of the field of view. However, the calibration results for the virtual patterns are still acceptable, since the reprojection errors are relatively small at low magnification values. It can be inferred that it is possible to end up with smaller reprojection errors under higher magnifications.

It is also observed from the tables that the computed radial distortion coefficients are very small. This proves that the microscope lenses are machined very precisely. Moreover, α and β angles have non-zero values which can be resulted from the imprecise manufactured mechanical components of the setup. These angles have to be considered during the manipulation tasks to have accurate results.

5.2.2 Online Calibration Results

To show the validity of the online calibration algorithm, it is implemented in the microassembly workstation. A square pattern on the sample stage is moved along a circular path in the x-y plane and one of its corner is tracked in subpixel accuracy at 30 Hz. Along the designed trajectory, the magnification is changed from 0.9X to 1.2X at the 50th iteration. Pixel coordinates of the image feature along the encoder output of the sample stage are used to test the online parameter estimation algorithm. The trajectory which is followed by the corner in the image and world coordinates are depicted in Fig. 5.9. Using the obtained trajectory information in the online

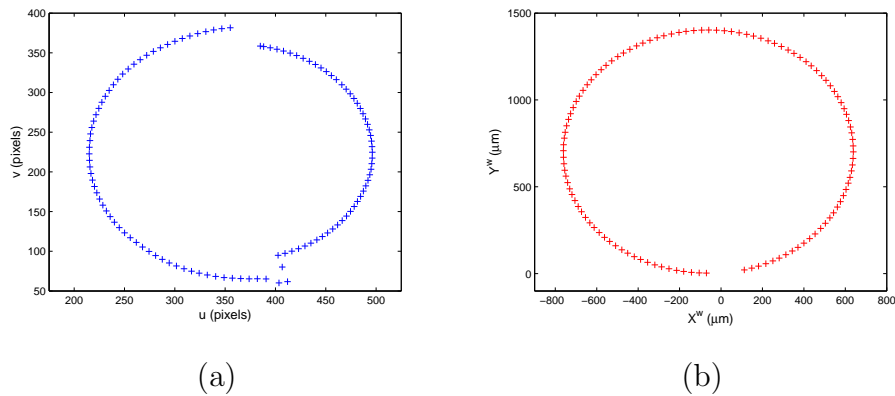


Figure 5.9: The Trajectory of the Corner in (a) Image and (b) World Coordinates

parameter estimation algorithm, the entries of the projection matrix are computed,

shown in Fig. 5.10. The evolution of the prediction error in (4.26) is computed

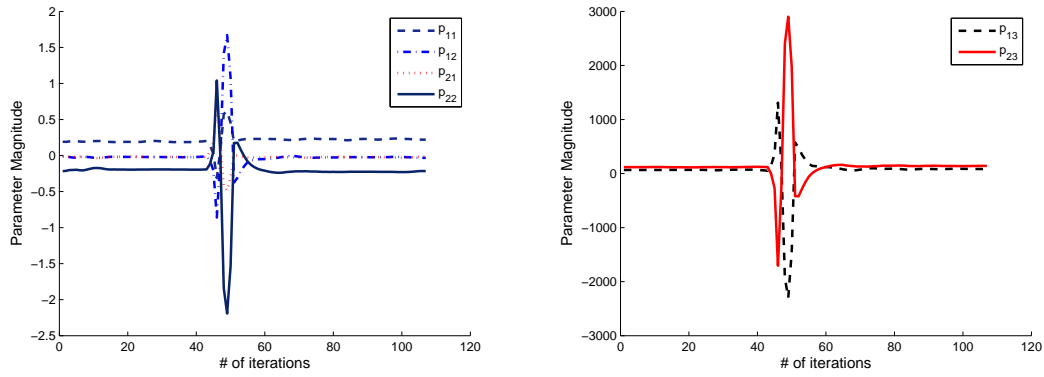


Figure 5.10: Estimated Entries of the Projection Matrix

using the estimated projection matrix and plotted in Fig. 5.11. It is shown that the

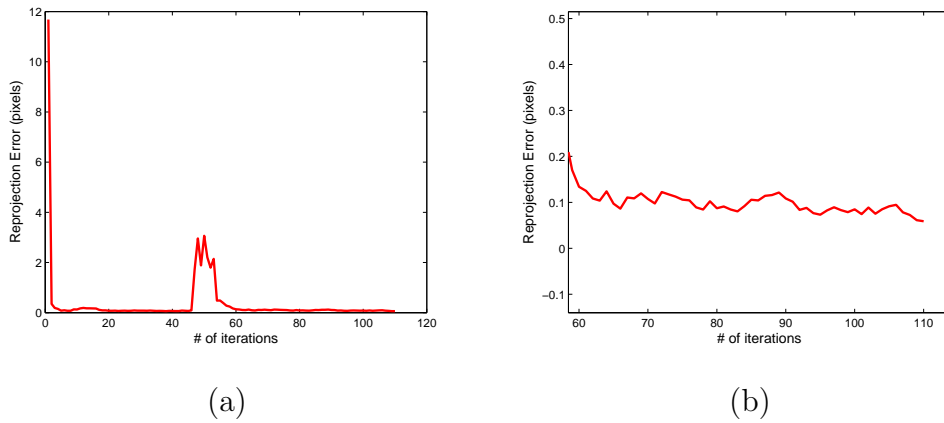


Figure 5.11: (a) Prediction Error (b) Zoomed Prediction Error

prediction error decays to 0.1 pixels after the magnification change. Once we have the projection matrix, we can obtain the optical system parameters using the method presented in Section 4.2. The computed magnification during the experiment is depicted in Fig. 5.12. It is observed that the proposed method converges to the new magnification value in 8 steps or 0.26 sec. In order to have shorter convergence time, the forgetting factor β is automatically increased to eliminate the effect of the past data, once the magnification motor turns. The convergence time could also be improved by increasing the speed of the magnification motor and thus providing a step response.

Note that there exist small variations in the computed magnification. Since the camera and the manipulator frames are not perfectly aligned, the Z coordinate of

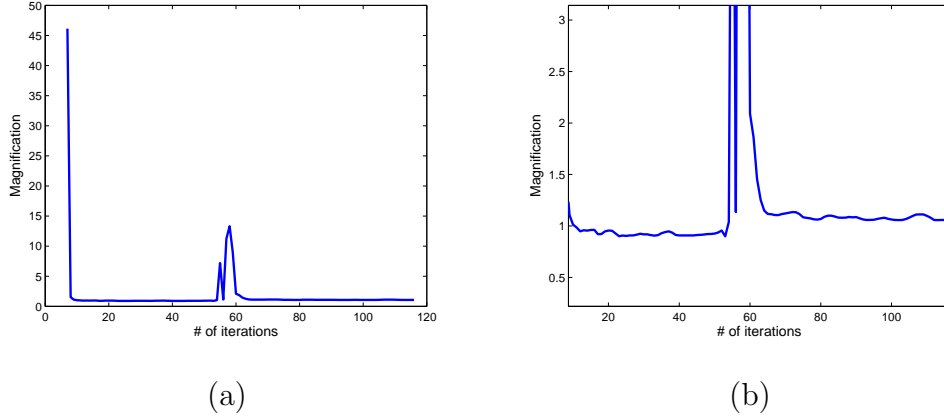


Figure 5.12: (a) Overall Magnification Plot (b) Zoomed Magnification Plot

the moving center in the objective frame may alter in a small range without getting blurred. Therefore, the calibration parameters can be modified during the motion.

Finally, it has been demonstrated that the proposed online calibration algorithm could adapt itself to the different operating modes through a recursive least square method. The presented method can be used in visually guided micromanipulation tasks to improve the accuracy of the vision based control structure. It can also be used in the applications which require the metric coordinates of the objects under an optical microscope without a priori information about the calibration parameters of the system.

5.2.3 Force Estimation Results

In order to evaluate the performance of the force estimation model, zebrafish embryos are chosen to be experimented. Due to its easily accessible eggs, high fertility, external fertilization and translucent embryos, zebrafish is preferred. In spite of their relatively large size (1.4 mm), zebrafish embryos have a delicate structure and small forces may create significant deformations on their membranes which is desirable for testing the proposed model. After the freshly harvested eggs are put on the sample stage in a petridish, a microgripper is employed to immobilize the embryo during the compression. Before the force sensing probe applies a uniaxial load compressing the biomembrane, the probe is aligned with the embryo in a way that the tangential forces are eliminated. An illustrative scene is shown in Fig. 5.13.

The experiments are conducted in room temperature (22-24°C). The force and

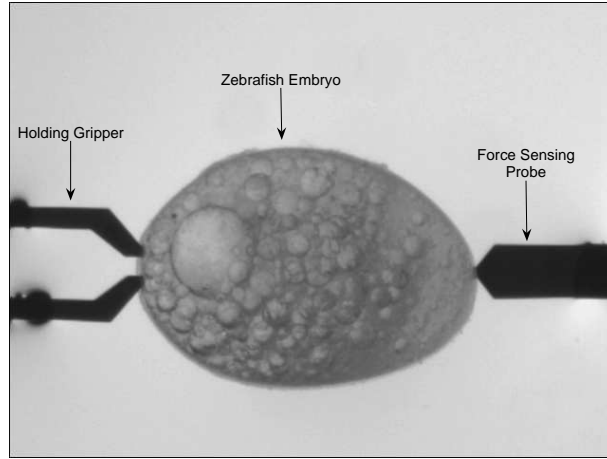


Figure 5.13: Zebrafish Embryos with Holding Gripper and Force Sensing Probe

deformation measurements are obtained at 30 Hz during the force loading. The probe moves to the center of the egg at $5 \mu\text{m}/\text{s}$ before the force reaches to the maximum of force sensing range and then returns to its initial position at the same velocity. Note that the acceleration of the contact point is zero except the direction changes. The force information is obtained from the capacitive force sensor embedded in the probe. The deformation and velocity of the contact point are calculated by the Lucas-Kanade optical flow estimation method [49] with subpixel accuracy.

The resulting force for the trapezoid displacement is illustrated in Fig. 5.14.

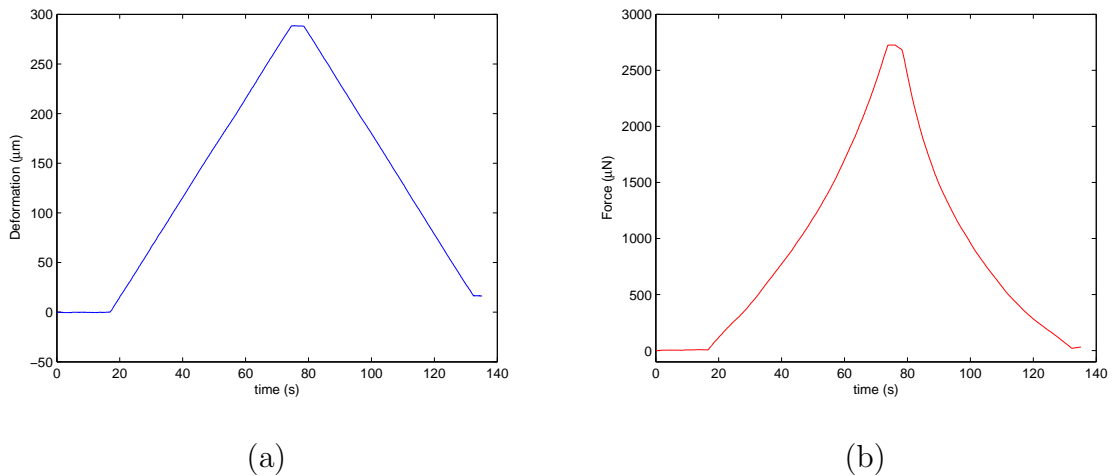


Figure 5.14: (a) Deformation (b) Force

Having measured the force during the experiment, the explicit solution for the model (4.44) gives the parameters as $\hat{k}_1 = 4.5161$, $\hat{k}_2 = 0.0001$, $\hat{b} = 27.7200$. The reconstructed force with the estimated parameters is shown in Fig. 5.15.

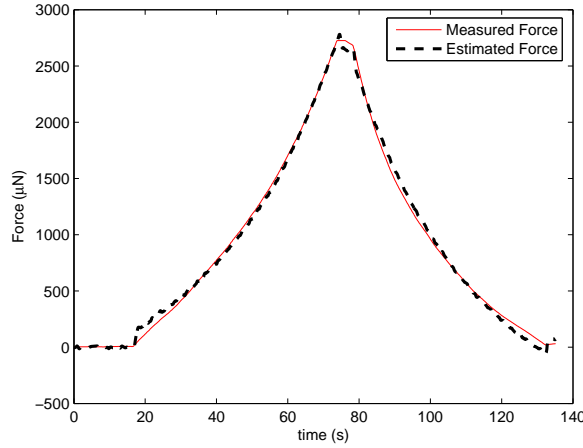


Figure 5.15: Measured and Reconstructed Force I

Although this estimation results in 3.89 percent error, modeling the second part of the force (after the velocity is negative) with the spring-mass-damper parameters may be inaccurate from a robotics point of view. Neglecting the damping effects in the second part, the unknown parameters can be estimated by fitting only the second part of force data to a mass-spring model. The damping coefficient can be obtained by relating the error with the velocity in the first part. The estimation yields the parameters, $\hat{k}_1 = 2.9577$, $\hat{k}_2 = 0.0001$, $\hat{b} = 51.3317$ with a 5.22 percent error. The resulting estimated force is illustrated in Fig. 5.16.

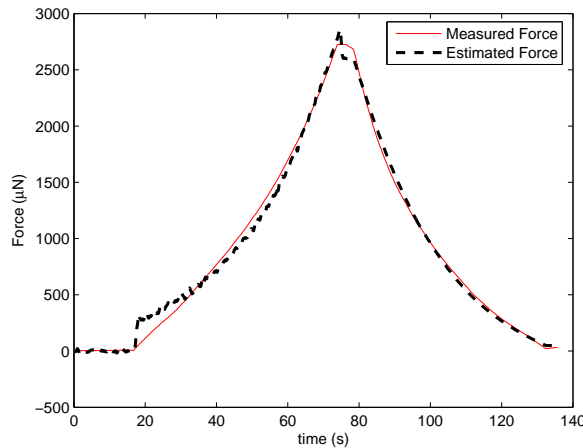


Figure 5.16: Measured and Reconstructed Force II

We can also fit the first part of the measured force into the model, estimate the three parameters and reconstruct the force by using three parameters for the first

part and assuming $b = 0$ for the second part. The error between the measured and estimated force is 10.72 percent of the measured one. The estimated parameters are $\hat{k}_1 = 5.8137$, $\hat{k}_2 = 4.33e - 5$, $\hat{b} = 7.9539$. The estimated force is shown in Fig. 5.17.

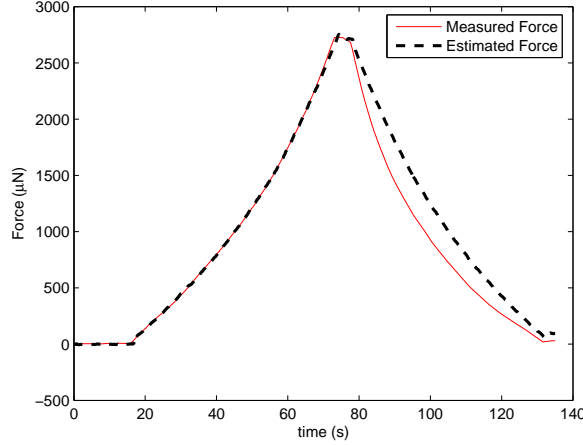


Figure 5.17: Measured and Reconstructed Force III

However, this method results in poor estimation result in the second part. This result may be explained with the observation that the membrane of the embryo is not recovering to its original position at the end of the manipulation. 25 micron offset is observed between the position of the contact point in the first and the last frame. The reason for that offset can be the fact that the holding gripper may be penetrated into the embryo, while the probe is pushing the embryo. This offset can be eliminated by modifying the displacement ($x(t)$)

$$x^*(t) = x(t) - 25(1 - e^{-\alpha t}) \quad (5.2)$$

which means that the offset is gradually becomes 25 microns. The resulting estimated force with the eliminated displacement ($x^*(t)$) is plotted in Fig. 5.18. The error becomes 3.6 percent of the measured force with the parameters $\hat{k}_1 = 5.8781$, $\hat{k}_2 = 3.8346e - 5$, $\hat{b} = 1.1834$.

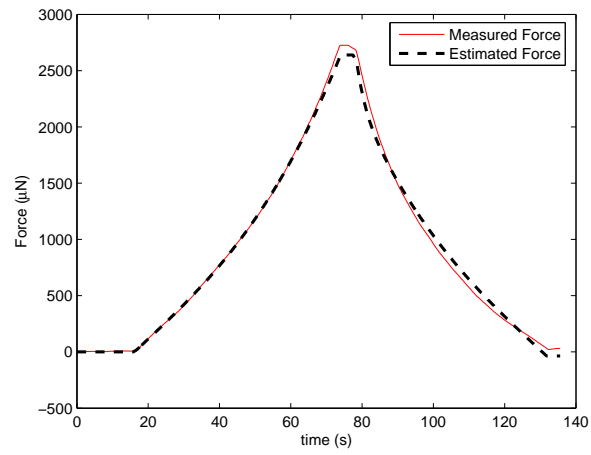


Figure 5.18: Measured and Reconstructed Force IV

Chapter 6

Conclusion

In this thesis it has been demonstrated that fully automated dexterous micromanipulations can be done at the precision of micron level using vision and force data. In order to effectively compensate the errors due to the uncertainties about the position, behavior and shape of the microobjects to be manipulated; the robust vision control structure is proposed and implemented. To realize the closed loop structure, real-time object and end-effector detection, optical system calibration, autofocus-ing, visual controller, force sensing and motion planner modules are developed. The details of the designed algorithms are presented in the third chapter.

Moreover, novel estimators are developed to identify the system and to characterize the mechanical properties of the biological structures through a synthesis of concepts from the computer vision, estimation and control theory. The computed mechanical parameters are utilized to estimate the imposed force on a biomembrane and to provide the adequate information to control the position, velocity and acceleration of the probe without damaging the cell or tissue during an injection task. The design of the observer is explained in the fourth chapter and the experimental results are shown in the fifth chapter.

With the work which is presented in this thesis, the theoretical and practical knowledge on micromanipulation at Sabanci University have been significantly enhanced. The previously presented the semi-automatic tasks [50], which uses dynamic look and move structure vision based control, have been improved by introduction of the full automated micromanipulation tasks which employ robust visual servoing schemes and the force feedback.

Based on the acquired research experience during this work, an insight was gained

on how to advance the present work in the microassembly workstation. Since the setup has the total of four degrees of freedom -linear motion along x, y, z axes and rotational motion around z axis-, it is not possible to execute the rotation around x and y axes. In order to manipulate more complex geometries in 3D, lacking rotational movement capabilities should be added to the manipulators. A further development can be done by the integration of motorized vision sensors to eliminate the disadvantages of small depth of field. Introducing new moving vision sensors may maximize the resolvability by ensuring focused and nonoccluded views in micromanipulation tasks.

Appendix A

Derivation of the Interaction Matrix

Let (X^o, Y^o, Z^o) denote the objective frame coordinates of an observed feature point P . Locating the image coordinate frame at the center of the CCD array and assuming weak perspective projection, the undistorted image coordinates (u', v') in objective frame are given as

$$u' \approx MX, v' \approx MY, \quad (\text{A.0.1})$$

where $M = \frac{f}{T_z}$ is the total magnification of the optical system.

Neglecting the lens radial distortion parameter (κ_1), the distorted image coordinates (u, v) in pixels can be written as

$$u \approx u' = \frac{M}{s_x} X^o, \quad v \approx v' = \frac{M}{s_y} Y^o \quad (\text{A.0.2})$$

where s_x and s_y are the effective pixel sizes.

Differentiation of (A.0.2) with respect to time implies

$$\dot{u} = \frac{M}{s_x} \dot{X}^o, \quad \dot{v} = \frac{M}{s_y} \dot{Y}^o \quad (\text{A.0.3})$$

Assume that the point P is rigidly attached to the end effector of the manipulator and moves with an angular velocity $\Omega = (\omega_x, \omega_y, \omega_z)$ and a translational velocity $V = (V_x, V_y, V_z)$. The motion in the objective frame is given by

$$\begin{pmatrix} \dot{X}^o \\ \dot{Y}^o \\ \dot{Z}^o \end{pmatrix} = \begin{pmatrix} V_x \\ V_y \\ V_z \end{pmatrix} + \begin{pmatrix} 0 & -\omega_z & \omega_y \\ \omega_z & 0 & -\omega_x \\ -\omega_y & \omega_x & 0 \end{pmatrix} \begin{pmatrix} X^o \\ Y^o \\ Z^o \end{pmatrix} \quad (\text{A.0.4})$$

Substituting (A.0.4) into (A.0.3) and using (A.0.2) implies

$$\begin{pmatrix} \dot{u} \\ \dot{v} \end{pmatrix} = \underbrace{\begin{pmatrix} \frac{M}{s_x} & 0 & 0 & 0 & \frac{M}{s_x} Z^o & -\frac{s_y}{s_x} v \\ 0 & \frac{M}{s_y} & 0 & -\frac{M}{s_y} Z^o & 0 & \frac{s_x}{s_y} u \end{pmatrix}}_{\triangleq L_s} \begin{pmatrix} V_x \\ V_y \\ V_z \\ \omega_x \\ \omega_y \\ \omega_z \end{pmatrix} \quad (\text{A.0.5})$$

where L_s is the interaction matrix for a point feature.

Bibliography

- [1] World Technology Evaluation Center, “MEMS/Microsystems Device and Process Technologies”, January 2000, http://www.wtec.org/loyola/mcc/mems_eu/Pages/Chapter-5.html.
- [2] L.J. Hombek, “Digital Light Processing and MEMS: Timely Convergence for a Bright Future (Invited Plenary Paper),” *SPIE Micromachining and Microfabrication*, Austin, Texas 1995 , 214-995-2426.
- [3] D. Pescovitz, “Solving the Hard Problems of Hard Disks”, 2003 <http://www.coe.berkeley.edu/labnotes/0603/horowitz.html>.
- [4] B. Kim, H. Kang, D.H. Kim, G.T. Park, J.O. Park, “Flexible Microassembly System based on Hybrid Manipulation Scheme”, *IEEE/RSJ Int. Conf. on Intelligent Robots and Systems*, Nevada, 2003, pp. 2061–2066.
- [5] G. Yang, J.A. Gaines, B.J. Nelson, “A flexible experimental workcell for efficient and reliable wafer-level 3D micro-assembly”, *IEEE Int. Conf. Robotics and Automation*, 2001, vol.1, pp. 133–138.
- [6] B.J Nelson, Y. Zhou and B. Vikramaditya, “Sensor-based microassembly of hybrid MEMS device”, *IEEE Control Systems*, 1998, pp.35–45.
- [7] F. Beyeler, D.J. Bell, B.J. Nelson, Y. Sun, A. Neild, S. Oberti and J. Dual, “Design of a Micro-Gripper and an Ultrasonic Manipulator for Handling Micron Sized Objects”, *Int. Conf. on Intelligent Robots and Systems*, Beijing, China, 2006, pp. 772–777.
- [8] N. Dechev, W. L. Cleghorn, and J. K. Mills, “Microassembly of 3-D MEMS structures utilizing a MEMS microgripper with a robotic manipulator”, *IEEE Int. Conf. on Robotics and Automation*, 2003, vol. 3, pp. 3193-3199.

- [9] D. O. Popa, B. J. Kang, J. Sin, and J. Zou, “Reconfigurable micro-assembly system for photonics applications”, *IEEE Int. Conf. on Robotics and Automation*, Washington, 2006, pp. 1495–1500.
- [10] Y. Sun, B.J. Nelson, “Microrobotic cell injection”, *Int. Conf. on Robotics and Automation*, 2001, vol.1, pp. 620–625.
- [11] Sun, Y. Wan, Kenneth, R.P., Bischof, J.C. and Nelson, B.J. Member, “Mechanical property characterization of mouse zona pellucida”, *IEEE Trans. on Nanobioscience*, 2003, vol. 2, no. 4, pp. 279–286.
- [12] X. Li, G. Zong, S. Bi, “Development of Global Vision System for Biological Automatic micromanipulation System”, *Int. Conf. on Robotics and Automation*, Seoul, 2001, pp. 127–132.
- [13] D.-H. Kim, C.N. Hwang, Y. Sun, S.H. Lee, B. Kim, B.J. Nelson, “Mechanical Analysis of Chorion Softening in Prehatching Stages of Zebrafish Embryos”, *IEEE Trans. on Nanobioscience*, 2006, vol. 5, no. 2, pp. 89–94.
- [14] W.H.Wang, X.Y. Liu, Y. Sun, “Autonomous Zebrafish Embryo Injection Using a Microrobotic System”, *Int. Conf. on Automation Science and Engineering*, 2007, pp. 363–368.
- [15] F. Dionnet, D.S. Haliyo, S. Regnier, “Autonomous micromanipulation using a new strategy of accurate release by rolling”, *IEEE Int. Conf. on Robotics and Automation*, 2004, vol. 5, pp. 5019–5024.
- [16] M. Sitti, “Controlled Pushing of Nanoparticles: Modeling and Experiments“, *IEEE/ASME Trans. on Mechatronics*, 2000, 5(2), pp. 199–221.
- [17] C. Pawashe, M. Sitti, “Two-Dimensional Vision-Based Autonomous Microparticle Assembly using Nanoprobes”, *Journal of Micromechatronics*, 2006, vol. 3, no. 3-5, pp. 285–306.
- [18] L. Ren, L. Wang, J.K. Mills, D. Sun, “3-D Automatic Microassembly by Vision-Based Control. *IEEE/RSJ Int. Conf. on Intelligent Robots and Systems*, San Diego, 2007, pp. 297–302.

- [19] K.-F. Bohringer, B.R. Donald, R. Mihailovich, N.C. MacDonald, “Sensorless manipulation using massively parallel microfabricated actuator arrays”, *IEEE Int. Conf. on Robotics and Automation*, 1998, pp. 826–833.
- [20] Z. Lu, P.C.Y. Chen, W. Lin, “Force Sensing and Control in Micromanipulation”, *IEEE Trans on Systems, Man, and Cybernetics Part C: Applications and Reviews*, 2006, vol. 36, NO. 6, pp. 713–724.
- [21] M. Kaneko, R. Kempf, Y. Kurita, Y. Iida, H. K. Mishima, H. Tsukamoto and E. Sugimoto, “Measurement and Analysis of Human Eye Excited by an Air Pulse”, *IEEE Int. Conf. on Multisensor Fusion and Integration for Intelligent Systems*, 2006, pp. 353–358.
- [22] M. Sitti, “Microscale and nanoscale robotics systems [Grand Challenges of Robotics]”, *IEEE Robotics and Automation Magazine*, vol. 14, pp. 53–60. (2007)
- [23] J. J. Abbott, Z. Nagy, F. Beyeler, and B. J. Nelson, “Robotics in the Small, Part I: Microrobotics”, *IEEE Robotics and Automation Magazine*, 2007, 14(2), pp.92–103.
- [24] T. Kasaya, H. Miyazaki, S. Saito, T. Sato, “Micro object handling under SEM by vision-based automatic control”, *IEEE Int. Conf. Robotics and Automation*, Detroit, 1999, pp. 2189-2196.
- [25] D. H. Kim, Y. Kim, K. Y. Kim, and S. M. Cha, “Dexterous teleoperation for micro parts handling based on haptic/visual interface”, *IEEE Int. Symp. Micromechatron. Human Sci.*, 2001, pp. 211-217.
- [26] A.C. Sanderson, L. Weiss, “Image-based visual servo control using graph error signals”, *IEEE Journal of Robotics and Automation*, 1980, pp. 1074-1077.
- [27] L. Weiss, A.C. Sanderson, C.P. Neuman, “Dynamic Sensor-Based Control of Robots with Visual Feedback”, *IEEE Journal on Robotics and Automation*, 1987, vol. 3, 5, pp. 404–417.

- [28] B. Espiau, F. Chaumette, P. Rives, “A New Approach to Visual Servoing in Robotics”, *IEEE Trans. on Robotics and Automation*, 1992, vol. 8, 3, pp. 313–326.
- [29] D. Kragic, “Visual Servoing for Manipulation: Robustness and Integration Issues”. Ph.D. Thesis, Computational Vision and Active Perception Laboratory (CVAP). 2001, Royal Institute of Technology, Stockholm, Sweden.
- [30] F. Chaumette, S. Hutchinson, “Visual servo control I. Basic approaches”, *IEEE Robotics & Automation Magazine*, Volume 13, Issue 4, Dec. 2006 Page(s):82 - 90.
- [31] K. Hashimoto, T. Ebine, K. Sakamoto, H. Kimura, “Full 3D Visual Tracking with Nonlinear Model-based Control, *American Control Conference*”, San Francisco, 1993, pp.n 3180–3184.
- [32] B.J. Nelson, N.P. Papanikolopoulos, P.K. Khosla, “Robotic Visual Servoing and Robotic Assembly Tasks”, *IEEE Robotics and Automation Magazine*, 1996, vol. 3, no. 2, pp 23–31.
- [33] J. Gangloff, M. Mathelin, G. Abba, “6 DOF High Speed Dynamic Visual Servoing Using GPC Controllers”, *IEEE Int. Conf. on Robotics and Automation*, 1998, pp. 2008–2013.
- [34] P. Martinet, C. Thibaud, D. Khadraoui, J. Gallice, “First Results Using Robust Controller Synthesis in Automatic Guided Vehicles Applications, *Third IFAC Symposium on Intelligent Autonomous Vehicles, IAV’98*, Madrid, 1998, vol. 1, pp 204–209.
- [35] E. Malis, “Visual servoing invariant to changes in camera intrinsic parameters”, *IEEE Trans. on Robotics and Automation*, 2004, vol. 20, pp. 72-81.
- [36] E. Krotkov and J.P. Martin, “Range from Focus”, *IEEE Int. Conf. on Robotics and Automation*, 1986, Vol. 3, pp.1093–1098.
- [37] Y. Sun, S. Duthaler and B.J. Nelson, “Autofocusing Algorithm Selection in Computer Microscopy” , *IEEE/RSJ Int. Conf. on Intelligent Robots and Systems (IROS)*, 2005, pp. 70–76.

- [38] Y. Xiong, S.A. Schafer, “Depth from Focusing and Defocusing”, *IEEE Computer Society Conf. on Computer Vision and Pattern Recognition*, 1993, pp. 68–73.
- [39] L. Ljung: “System Identification - Theory For the User”, 2nd ed, PTR Prentice Hall, Upper Saddle River, N.J., 1999.
- [40] R.E. Kalman, “A New Approach to Linear Filtering and Prediction Problems”, *Trans. of the ASME Journal of Basic Engineering*, 1960, pp. 35–45.
- [41] Tsai, R.Y.: “A Versatile Camera Calibration Technique for High-Accuracy 3D Machine Vision Metrology Using Off-the-Shelf TV Cameras and Lenses”, *IEEE Journal of Robotics and Automation*, 1987, vol. 3, pp. 323–344.
- [42] Zhang, Z.Y.: “Flexible Camera Calibration by Viewing a Plane from Unknown Orientations”, *IEEE Int. Conf. on Computer Vision*, 1999, pp. 666–673.
- [43] Caprile, B., Torre, V.: “Using Vanishing Points for Camera Calibration”, *International Journal on Computer Vision*, 1990, vol. 4, pp. 127–140.
- [44] H. Zhuang and W. C. Wu, “Camera Calibration with a Near-Parallel Calibration Board Configuration”, *IEEE Trans. on Robotics and Automation*, 1996, vol. 12, pp. 918–921.
- [45] Y. Zhou, B.J. Nelson, “Calibration of a parametric model of an optical microscope”, *Optical Engineering*, 1999, vol. 38, pp. 1989–1995.
- [46] Ammi, M., Fremont, V., Ferreira, A. “Flexible Microscope Calibration using Virtual Pattern for 3-D Telemicromanipulation”, 2005, *IEEE Trans. on Robotics and Automation*, pp. 3888–3893.
- [47] M.A. Greminger, B.J. Nelson, “Vision-based force measurement”, *IEEE Trans. on Pattern Analysis and Machine Intelligence*, 2004, vol. 26, 3, pp. 290–298.
- [48] J. Flusser, B. Zitova, “Invariants to Convolution with Circularly Symmetric PSF”, *IEEE Int. Conf. on Pattern Recognition*, 2004, pp. 11–14.

- [49] B.D. Lucas, T. Kanade, “An iterative image registration technique with an application to stereo vision”, *Imaging Understanding Workshop*, 1981, pp 121–130.
- [50] E. Dogan, “Design and Implementation of a Vision System for Microassembly Workstation”, MSc Thesis, Sabanci University, Turkey, 2006.